

Effective field theory analysis of rare $|\Delta c| = |\Delta u| = 1$ charm decays

Hector Gisbert,^{a,b,c} Gudrun Hiller^d and Dominik Suelmann^d

^a*Escuela de Ciencias, Ingeniería y Diseño, Universidad Europea de Valencia, Passeig de la Petxina 2, 46008 Valencia, Spain*

^b*Istituto Nazionale di Fisica Nucleare (INFN), Sezione di Padova, Via F. Marzolo 8, 35131 Padova, Italy*

^c*Dipartimento di Fisica e Astronomia ‘G. Galilei’, Università di Padova, Via F. Marzolo 8, 35131 Padova, Italy*

^d*TU Dortmund University, Department of Physics, Otto-Hahn-Str.4, D-44221 Dortmund, Germany*

E-mail: hector.gisbert@universidadeuropea.es,
ghiller@physik.uni-dortmund.de, dominik.suelmann@tu-dortmund.de

ABSTRACT: We perform a global analysis of $|\Delta c| = |\Delta u| = 1$ transitions using recent data on $D^0 \rightarrow \mu^+ \mu^-$, $D^+ \rightarrow \pi^+ \mu^+ \mu^-$, $\Lambda_c \rightarrow p \mu^+ \mu^-$, and $D^0 \rightarrow \pi^+ \pi^- \mu^+ \mu^-$ decays, and work out constraints on new physics Wilson coefficients $\mathcal{C}_{7,9,10}^{(\prime)}$. While results are consistent with the standard model, we find sizeable room for new physics that can be cleanly signaled with null test observables, not probed with searches in other sectors such as kaon and b -decays. The decay $D^0 \rightarrow \pi^+ \pi^- \mu^+ \mu^-$ requires better understanding of hadronic contributions to be competitive in the current fit. Progress can be achieved by precision study of the double differential decay rate in the dipion and dimuon masses, together with improved theory modelling and $D \rightarrow \pi\pi$ transition form factors. On the other hand, the 4-body decay is an important contributor to the future global analysis due to its angular distributions that probe complementary combinations of Wilson coefficients, and as a QCD laboratory. The decay $\Lambda_c \rightarrow p \ell^+ \ell^-$ is the rising star due to the simplicity of a 3-body decay with available form factors from lattice QCD, sensitivity to both 4-fermion and electromagnetic dipole couplings and its null test forward-backward asymmetry.

Contents

1	Introduction	2
2	Effective Theory Framework	3
3	Rare charm decays	5
3.1	$D \rightarrow \ell^+ \ell^-$ and $D \rightarrow \pi \ell^+ \ell^-$	5
3.2	$\Lambda_c \rightarrow p \ell^+ \ell^-$	7
3.2.1	Modelling resonances	8
3.2.2	Limits on NP	9
3.3	$D \rightarrow P_1 P_2 \ell^+ \ell^-$	11
3.3.1	Full angular distribution	11
3.3.2	CP-symmetries and asymmetries	15
4	Phenomenological analysis of $D^0 \rightarrow \pi^+ \pi^- \mu^+ \mu^-$ observables	16
4.1	Fitting resonance parameters	17
4.2	Fits to NP in different scenarios	20
4.3	Beyond S- and P-wave	23
5	Global $c \rightarrow u$ fits	23
5.1	One-dimensional fits	24
5.2	Two-dimensional fits	24
6	Future prospects	26
6.1	$\Lambda_c \rightarrow p \ell^+ \ell^-$ physics potential	27
6.2	Complementarity	30
7	Conclusions	30
A	Form factors	33
A.1	Non-resonant form factors	33
A.2	Resonant form factors	33
A.2.1	P-wave	34
A.2.2	S-wave	34
B	$D \rightarrow P_1 P_2 \ell^+ \ell^-$ angular observables	34
C	Input for SM and NP fits	37

1 Introduction

Flavor-changing neutral currents (FCNCs) are suppressed in the Standard Model (SM) by the Glashow-Iliopoulos-Maiani (GIM) mechanism, an intricate interplay of the fermion masses and mixings. The suppression is parametrically enhanced for up-type quarks. Together with the rich set of couplings at work in radiative, semileptonic and dineutrino decay modes and the experimental prospects at high luminosity flavor facilities, such as LHCb [1], Belle II [2], BES III [3], and possible future machines [4, 5] this singles out SM tests with FCNC decays of charmed hadrons.

Charm physics is notoriously challenging due to resonance pollution and the unfortunate value of the charm quark which sits between the nominal regions of validity of effective field theories for light quarks and heavy quarks. Instead, sensitivity to new physics (NP) comes from approximate symmetries of the SM. Notably, the efficient GIM-suppression [6–8] gives directions to systematically identify clean null test observables from angular distributions of D -mesons [9] and charm baryons [10].

In this study we present the first global analysis of rare $|\Delta c| = |\Delta u| = 1$ charm decays, based on $D^0 \rightarrow \mu^+\mu^-$, $D^+ \rightarrow \pi^+\mu^+\mu^-$, $\Lambda_c \rightarrow p\mu^+\mu^-$, and $D^0 \rightarrow \pi^+\pi^-\mu^+\mu^-$. We take advantage of the novel theory proposals to test the SM, hadronic input from lattice QCD [11, 12] including recent data from the LHC [13, 14] to extract limits on the Wilson coefficients governing $c \rightarrow u\mu^+\mu^-$ transitions.

While the null tests are able to signal NP, the interpretation of the data in terms of NP, specifically when one aims to obtain limits, is affected by hadronic backgrounds. We discuss this for angular null test observables in $\Lambda_c \rightarrow p\mu^+\mu^-$, and $D^0 \rightarrow \pi^+\pi^-\mu^+\mu^-$ decays. We furthermore analyze the impact of binning in the dilepton invariant mass on the NP reach.

The paper is organized as follows: We give the weak effective theory framework in Sec. 2. We present decay modes and their angular observables in Sec. 3. We also work out constraints from recent data on the branching ratio of $\Lambda_c \rightarrow p\mu^+\mu^-$ decays. The phenomenological analysis and extraction of limits from data on the 4-body $D^0 \rightarrow \pi^+\pi^-\mu^+\mu^-$ decays is given in Sec. 4. The results of the global $c \rightarrow u\mu^+\mu^-$ fit are presented in Sec. 5. In Sec. 6 we study the future prospects for $\Lambda_c \rightarrow p\mu^+\mu^-$ decays and the physics potential of the forward-backward asymmetry for SM tests. We investigate the impact of binning in the dilepton mass and discuss the complementarity with other rare charm null test observables. In Sec. 7 we conclude. Auxiliary information on form factors and the $D^0 \rightarrow \pi^+\pi^-\mu^+\mu^-$ angular observables is provided in the appendix.

2 Effective Theory Framework

We give the weak effective theory framework for semileptonic $|\Delta c| = |\Delta u| = 1$ transitions. They are described by the effective low energy Hamiltonian [7, 8, 15, 16]

$$\mathcal{H}_{\text{eff}} = -\frac{4G_F}{\sqrt{2}} \frac{\alpha_e}{4\pi} \left[\sum_{q=d,s} \lambda_q \sum_{i=1,2} c_i^{(q)}(\mu) \mathcal{O}_i^{(q)}(\mu) + \sum_{i \neq T, T_5} \left(c_i(\mu) \mathcal{O}_i(\mu) + c'_i(\mu) \mathcal{O}'_i(\mu) \right) + \sum_{i=T, T_5} c_i(\mu) \mathcal{O}_i(\mu) \right], \quad (2.1)$$

with dimension-six operators [17–19]

$$\begin{aligned} \mathcal{O}_2^{(q)} &= (\bar{u}_L \gamma_\mu q_L)(\bar{q}_L \gamma^\mu c_L), & \mathcal{O}_1^{(q)} &= (\bar{u}_L \gamma_\mu T^a q_L)(\bar{q}_L \gamma^\mu T^a c_L), \\ \mathcal{O}_7 &= \frac{m_c}{e} (\bar{u}_L \sigma_{\mu\nu} c_R) F^{\mu\nu}, & \mathcal{O}_8 &= \frac{m_c g_s}{e^2} (\bar{u}_L \sigma_{\mu\nu} T^a c_R) G_a^{\mu\nu}, \\ \mathcal{O}_9 &= (\bar{u}_L \gamma_\mu c_L)(\bar{\ell} \gamma^\mu \ell), & \mathcal{O}_{10} &= (\bar{u}_L \gamma_\mu c_L)(\bar{\ell} \gamma^\mu \gamma_5 \ell), \\ \mathcal{O}_{S(P)} &= (\bar{u}_L c_R)(\bar{\ell}(\gamma_5)\ell), & \mathcal{O}_{T(T_5)} &= \frac{1}{2} (\bar{u} \sigma_{\mu\nu} c)(\bar{\ell} \sigma^{\mu\nu}(\gamma_5)\ell). \end{aligned} \quad (2.2)$$

Here, $q_{L,R} = \frac{1}{2}(1 \mp \gamma_5)q$ represent the chiral quark fields, $\sigma^{\mu\nu} = \frac{i}{2}[\gamma^\mu, \gamma^\nu]$, T^a denote the generators of $SU(3)_C$ and g_s is the strong coupling constant. G_F denotes Fermi's constant and $\lambda_q = V_{cq}^* V_{uq}$, where V_{cq} and V_{uq} are elements of the Cabibbo-Kobayashi-Maskawa (CKM) matrix. The fine-structure constant, with the electromagnetic coupling e , reads $\alpha_e = e^2/(4\pi)$. The field strength tensors of the electromagnetic and gluonic fields are denoted by $F^{\mu\nu}$ and $G_a^{\mu\nu}$, respectively, where $a = 1, \dots, 8$.

Primed operators \mathcal{O}'_i are obtained from the \mathcal{O}_i by swapping the chiral projectors of the quark fields $L(R) \rightarrow R(L)$. We distinguish the purely NP contribution to the Wilson coefficients \mathcal{C}_i (capital letter) from the total one c_i (small letter) as $c_i^{(\prime)} = \mathcal{C}_i^{(\prime)\text{SM}} + \mathcal{C}_i^{(\prime)}$, with the SM coefficients denoted by $\mathcal{C}_i^{(\prime)\text{SM}}$. In the SM and, more general in models with minimal flavor violation, the primed coefficients are suppressed by m_u/m_c , the ratio of up to charm mass, which is negligible. Scalar, pseudoscalar and tensor operators also vanish in the SM, $\mathcal{C}_{S,P}^{(\prime)\text{SM}} = \mathcal{C}_{T,T_5}^{\text{SM}} = 0$.

In the SM $c \rightarrow u\gamma, \ell^+ \ell^-$ induced decays are dominated by contributions from the four-quark operators $\mathcal{O}_{1,2}^{(q)}$. They enter with single Cabibbo-suppression, see the corresponding CKM-factors λ_q . The other Wilson coefficients are protected by the GIM-mechanism, and vanish at the weak scale μ_W . $\mathcal{O}_{1,2}^{(q)}$ are induced by tree-level W -boson exchange at μ_W , and mix under QCD and running to the b -quark scale. At the b -quark mass scale the b -quark is integrated out, and contributions to $\mathcal{O}_{7,8,9}$ and additional four-quark penguin operators, not spelled out explicitly in (2.2) and negligible for $c \rightarrow u\ell^+ \ell^-$ transitions, are induced. The coefficients are then evolved to the charm mass scale, $\mu = m_c$ [8, 16, 20]. While the coefficients of $\mathcal{O}_{1,2}^{(q)}$ are order one, and all others assume sub-few percent yet finite values, the coefficient of \mathcal{O}_{10} remains protected, $\mathcal{C}_{10}^{\text{SM}} = 0$. Finite contributions to \mathcal{O}_{10} are expected at higher order in the electromagnetic interaction [9]. Effects are estimated at about per mille level, which is far beyond experimental sensitivity.

The operators $\mathcal{O}_{7,9}$ also receive perturbative contributions from matrix elements of four-quark operators involving electromagnetic and gluonic corrections, included in effective coefficients. At $\mu = m_c$, and at next-to-next-to-leading order (NNLO) they assume the following values [8, 20],

$$|\mathcal{C}_9^{\text{eff}}(q^2)| \lesssim \mathcal{O}(0.1) \quad (\lesssim 0.01), \quad |\mathcal{C}_7^{\text{eff}}(q^2)| \lesssim 0.01 \quad (\simeq \mathcal{O}(0.001)), \quad (2.3)$$

with entries in parentheses specific to the region of high dilepton invariant mass squared, $q^2 \gtrsim 1 \text{ GeV}^2$. These are all small and subdominant for SM phenomenology.

We also mention additional contributions worked out in the framework of QCD factorization, notably weak annihilation for $D \rightarrow \rho \ell^+ \ell^-$ [21], $D^+ \rightarrow \pi^+ \ell^+ \ell^-$ [22], and multibody radiative decays $D \rightarrow P_1 P_2 \gamma$, $P_{1,2} = \pi, K$ [23]. The annihilation of a charged (neutral) D meson into a W -boson is color favored (suppressed), hence larger for D^\pm and D_s than D^0 decays. Quantitatively, it has only a subleading effect in the $D^+ \rightarrow \pi^+ \mu^+ \mu^-$ analysis [22] with current experimental binning and accuracy [24]. Significant corrections are also expected on general grounds due to the small separation between the charm quark mass and the scale of QCD.

The phenomenology of $c \rightarrow u \ell^+ \ell^-$ transitions in the SM is governed by resonance contributions. These are predominantly sourced by charged-current operators $\mathcal{O}_{1,2}^{(q)}$, which have order one Wilson coefficients and give large rates of charm to light hadrons. The latter can decay electromagnetically to $\ell^+ \ell^-$, such as the ρ, ω , or ϕ -mesons, and therefore effectively contribute to \mathcal{O}_9 with coefficient denoted by \mathcal{C}_9^R . Due to their non-perturbative nature, these long-distance, resonant effects pose a challenge in controlling decay amplitudes and require improved data-driven modelling.

We model resonances with a phenomenological Breit-Wigner ansatz, fitting parameters to data. An alternative way would be to use data on the cross section of $e^+ e^-$ to hadrons plus dispersion relations, and assuming factorization, a method put forward by [25]. Historically, it has been employed in rare B -decays to avoid double-counting of short- and long-distance contributions to \mathcal{O}_9 . However, in rare charm decays, the short-distance contribution is essentially negligible, so this not an issue here. Recent analysis also reveals significant uncertainties from the dispersive analysis [22]. In addition, pseudoscalar resonances such as η, η' decaying to $\ell^+ \ell^-$ are not included. We therefore employ the simpler, yet flexible ansatz to explore the phenomenology of $\Lambda_c \rightarrow p \mu^+ \mu^-$ decays, and in particular, the 4-body $D^0 \rightarrow \pi^+ \pi^- \mu^+ \mu^-$ decays. The latter has resonance structure not just in the dilepton mass, hence requires further modelling beyond the approach [25] anyway.

We study observables that are especially sensitive to physics beyond the SM. The key feature to do so, which sets charm FCNCs apart from those in the kaon and B -sector is the GIM-protection of \mathcal{C}_{10} , and that the operators $\mathcal{O}_{10}, \mathcal{O}'_{10}$, characterized by an axial-vector coupling in the leptonic sector, are not switched on by QCD. In essence, this nullifies $V - A$ structure at low energies within the SM and observables proportional to this operator vanish [9]. This opportunity invites dedicated searches with concrete null test observables in $D^0 \rightarrow \pi^+ \pi^- \mu^+ \mu^-$ [9] and $\Lambda_c \rightarrow p \mu^+ \mu^-$ [26] decays.

3 Rare charm decays

We discuss the $c \rightarrow u \ell^+ \ell^-$ decay modes considered in the global analysis. The present best bounds from semileptonic decays stem from muons. However, we give the distributions for $\ell = e, \mu$. Tau-pairs are too heavy to be produced in the decays of charmed hadrons with the sole exception of the lepton-flavor violating decay $D \rightarrow e\tau$.

In Sec. 3.1 we discuss $D^0 \rightarrow \mu^+ \mu^-$ and $D \rightarrow \pi \mu^+ \mu^-$ decays and give the current limits on Wilson coefficients. We discuss baryonic $\Lambda_c \rightarrow p \mu^+ \mu^-$ decays and work out constraints on the Wilson coefficients using recent data from LHCb in Sec. 3.2. Distributions of 4-body $D^0 \rightarrow \pi^+ \pi^- \mu^+ \mu^-$ decays, which have the richest angular structure and offer the most observables from full angular analysis are given in Sec. 3.3. Due to its complicated nature we perform the phenomenological analysis and extractions of limits in Sec. 4.

We focus on NP effects from semileptonic and radiative operators $\mathcal{O}_{7,9,10}^{(\prime)}$, but give here also limits on scalar, pseudoscalar and tensor operators.

3.1 $D \rightarrow \ell^+ \ell^-$ and $D \rightarrow \pi \ell^+ \ell^-$

The double differential distribution of $D \rightarrow P \ell^+ \ell^-$, $P = \pi, K$ decays can be written as [27]

$$\frac{d^2\Gamma}{dq^2 d\cos\theta_\ell} = a(q^2) + b(q^2) \cos\theta_\ell + c(q^2) \cos^2\theta_\ell, \quad (3.1)$$

where θ_ℓ is the angle between the momentum of the ℓ^+ and the negative direction of flight of the parent D -meson in the dilepton $\ell^+ \ell^-$ rest frame. The distribution (3.1) leads to null test observables of the SM, the forward-backward asymmetry of the lepton pair

$$A_{\text{FB}}^{D \rightarrow P \ell \ell}(q^2) = \frac{1}{\Gamma} \left[\int_0^1 - \int_{-1}^0 \right] \frac{d^2\Gamma}{dq^2 d\cos\theta_\ell} d\cos\theta_\ell = \frac{b(q^2)}{\Gamma}, \quad (3.2)$$

and the ‘‘flat’’ term,

$$F_H(q^2) = \frac{2}{\Gamma} (a(q^2) + c(q^2)). \quad (3.3)$$

$A_{\text{FB}}^{D \rightarrow P \ell \ell}$ and F_H are normalized to the decay rate Γ , which in general depends on the q^2 -bin, $q^2 \in [q_{\text{min}}^2, q_{\text{max}}^2]$,

$$\Gamma = \int_{q_{\text{min}}^2}^{q_{\text{max}}^2} dq^2 \int_{-1}^1 \frac{d^2\Gamma}{dq^2 d\cos\theta_\ell} d\cos\theta_\ell = 2 \int_{q_{\text{min}}^2}^{q_{\text{max}}^2} dq^2 \left(a(q^2) + \frac{c(q^2)}{3} \right). \quad (3.4)$$

Explicit expressions for the angular functions a, b, c in terms of the NP Wilson coefficients are given in Ref. [28]. $F_H(q^2)$ and $A_{\text{FB}}^{D \rightarrow P \ell \ell}(q^2)$ are sensitive to (pseudo-)scalar and tensor operators. None of them is measured.

The most stringent constraint on $D \rightarrow P \ell^+ \ell^-$ branching ratios is $\mathcal{B}(D^+ \rightarrow \pi^+ \mu^+ \mu^-) < 6.7 \cdot 10^{-8}$ @ 90% C.L. from LHCb [24] in the full- q^2 region, $4m_\mu^2 \leq q^2 \leq (m_D - m_\pi)^2$, where m_D , m_π and m_ℓ denote mass of the D -meson, pion and lepton $\ell = e, \mu$, respectively.¹ We

¹Ref. [24] excluded the resonant region $\sqrt{q^2} \in [0.525, 1.250]$ GeV and extrapolated to obtain the limits for the full- q^2 region.

obtain

$$\begin{aligned}
& 1.2 |\mathcal{C}_7|^2 + 1.4 |\mathcal{C}_9|^2 + 1.4 |\mathcal{C}_{10}|^2 + 2.8 |\mathcal{C}_S|^2 \\
& + 2.8 |\mathcal{C}_P|^2 + 0.4 |\mathcal{C}_T|^2 + 0.3 |\mathcal{C}_{T_5}|^2 + 0.6 \operatorname{Re} [\mathcal{C}_9 \mathcal{C}_T^*] \\
& + 1.1 \operatorname{Re} [\mathcal{C}_{10} \mathcal{C}_P^*] + 2.6 \operatorname{Re} [\mathcal{C}_7 \mathcal{C}_9^*] + 0.6 \operatorname{Re} [\mathcal{C}_7 \mathcal{C}_T^*] \lesssim 1,
\end{aligned} \tag{3.5}$$

using $D \rightarrow \pi$ lattice form factors [12, 29]. Contributions from primed Wilson coefficients have not been spelled out to avoid clutter but they can be included by replacing $\mathcal{C}_i \rightarrow \mathcal{C}_i + \mathcal{C}'_i$. Results are consistent with previous analyses [22, 28, 30].

The purely leptonic decay $D^0 \rightarrow \ell^+ \ell^-$ offers complementary information to $D \rightarrow P \ell^+ \ell^-$ as it is sensitive to the difference $\mathcal{C}_{10,S,P} - \mathcal{C}'_{10,S,P}$ of Wilson coefficients,

$$\begin{aligned}
\mathcal{B}(D^0 \rightarrow \ell^+ \ell^-) &= \frac{G_F^2 \alpha_e^2 m_D^5 f_D^2}{64 \pi^3 m_c^2 \Gamma_D} \sqrt{1 - \frac{4 m_\ell^2}{m_D^2}} \left[\left(1 - \frac{4 m_\ell^2}{m_D^2}\right) |\mathcal{C}_S - \mathcal{C}'_S|^2 \right. \\
&\quad \left. + \left| \mathcal{C}_P - \mathcal{C}'_P + \frac{2 m_\ell m_c}{m_D^2} (\mathcal{C}_{10} - \mathcal{C}'_{10}) \right|^2 \right] + \mathcal{B}_{\text{LD}}.
\end{aligned} \tag{3.6}$$

Here, the leading long-distance contribution \mathcal{B}_{LD} comes from two-photon intermediate states and can be related to the decay $D^0 \rightarrow \gamma\gamma$ [6]. Using $\mathcal{B}(D^0 \rightarrow \gamma\gamma) < 8.5 \cdot 10^{-7}$ @ 90% C.L. by Belle [31] one obtains $\mathcal{B}_{\text{LD}}(D^0 \rightarrow \mu^+ \mu^-) < 4 \cdot 10^{-11}$. This is about two orders of magnitude below the upper limit @ 90% C.L. by CMS [14]

$$\mathcal{B}(D^0 \rightarrow \mu^+ \mu^-) < 2.2 \cdot 10^{-9}, \tag{3.7}$$

which yields

$$|\mathcal{C}_{10} - \mathcal{C}'_{10}| < 0.52, \tag{3.8}$$

where we used the value of the D -meson decay constant $f_D = 209.0 \pm 2.4 \text{ MeV}$ [32]. The SM estimate $\mathcal{B}_{\text{SM}}(D^0 \rightarrow \gamma\gamma) \sim 10^{-8}$ [6, 33] corresponding to $\mathcal{B}_{\text{SM}}(D^0 \rightarrow \mu^+ \mu^-) \sim 10^{-12}$ is even lower albeit with large theoretical uncertainties. Therefore, \mathcal{B}_{LD} can be safely neglected but it ultimately limits the sensitivity to test $\mathcal{C}_{10} - \mathcal{C}'_{10}$ below ~ 0.01 . Assuming that only $\mathcal{C}_{10}, \mathcal{C}'_{10}$ contributions are present in Eq. (3.5) it follows $|\mathcal{C}_{10} + \mathcal{C}'_{10}| \lesssim 0.85$. Combination with Eq. (3.8) allows one to put limits on the individual coefficients as

$$|\mathcal{C}_{10}|, |\mathcal{C}'_{10}| \lesssim 0.7. \tag{3.9}$$

Similarly, combining $(|\mathcal{C}_S + \mathcal{C}'_S|^2 + |\mathcal{C}_P + \mathcal{C}'_P|^2)^{1/2} < 0.60$ from Eq. (3.5) with

$$(|\mathcal{C}_S - \mathcal{C}'_S|^2 + |\mathcal{C}_P - \mathcal{C}'_P|^2)^{1/2} < 0.04, \tag{3.10}$$

from (3.7) and the charm MS-bar mass at the charm mass scale $m_c(\mu_c) \simeq 1.27 \text{ GeV}$ we obtain for the pseudo-scalar and scalar Wilson coefficients

$$|\mathcal{C}_S|, |\mathcal{C}'_S|, |\mathcal{C}_P|, |\mathcal{C}'_P| \lesssim 0.4. \tag{3.11}$$

The bound (3.10) is an order of magnitude stronger than the one on the vector operators Eq. (3.8), as it is not affected by chiral suppression $\sim m_\mu/m_D$. Tensor operators are bounded by $D^+ \rightarrow \pi^+ \mu^+ \mu^-$ decays, see Eq. (3.5), as follows

$$|\mathcal{C}_T| \lesssim 1.6, |\mathcal{C}_{T_5}| \lesssim 1.8. \tag{3.12}$$

3.2 $\Lambda_c \rightarrow p \ell^+ \ell^-$

The double differential distribution for $\Lambda_c \rightarrow p \ell^+ \ell^-$ can be written as [26]

$$\frac{d^2\Gamma}{dq^2 d\cos\theta_\ell} = \frac{3}{2} (K_{1ss}(q^2) \sin^2\theta_\ell + K_{1cc}(q^2) \cos^2\theta_\ell + K_{1c}(q^2) \cos\theta_\ell) . \quad (3.13)$$

Here, θ_ℓ is defined as the angle between the negative direction of flight of the parent charm baryon and the ℓ^+ in the dilepton center of mass frame. The differential decay rate is obtained after integrating over the lepton angle as

$$\frac{d\Gamma}{dq^2} = \int_{-1}^1 \frac{d^2\Gamma}{dq^2 d\cos\theta_\ell} d\cos\theta_\ell = 2 K_{1ss}(q^2) + K_{1cc}(q^2) . \quad (3.14)$$

In addition, baryonic $\Lambda_c \rightarrow p \ell^+ \ell^-$ decays give rise to angular observables A_{FB} and F_L

$$A_{\text{FB}}(q^2) = \frac{3}{2} \frac{K_{1c}(q^2)}{2K_{1ss}(q^2) + K_{1cc}(q^2)} , \quad F_L(q^2) = \frac{2K_{1ss}(q^2) - K_{1cc}(q^2)}{2K_{1ss}(q^2) + K_{1cc}(q^2)} , \quad (3.15)$$

Additional observables exist if the Λ_c 's are polarized [10]. In case they are polarized, for instance if originating from Λ_b - or Z -decays but the polarization is not measured, the differential distribution (3.13) remains the same. The dilepton mass squared is kinematically limited to be within $4m_\ell^2 \leq q^2 \leq (m_{\Lambda_c} - m_p)^2$, where m_{Λ_c} (m_p) denotes the Λ_c (proton) mass.

The longitudinal polarization fraction obeys $0 \leq F_L(q^2) \leq 1$. Together with (3.14) one finds that

$$0 \leq K_{1cc}(q^2) \leq \frac{1}{2} \frac{d\Gamma}{dq^2} , \quad \frac{1}{4} \frac{d\Gamma}{dq^2} \leq K_{1ss}(q^2) \leq \frac{1}{2} \frac{d\Gamma}{dq^2} . \quad (3.16)$$

The NP coefficients are encoded in the angular functions K_{1ss} , K_{1cc} , and K_{1c} , see Ref. [26] for details. The baryonic decay mode is phenomenologically richer than $D \rightarrow P \ell^+ \ell^-$ due to the higher spin. In particular, the angular functions receive contributions from both $\mathcal{C}_i + \mathcal{C}'_i$ and $\mathcal{C}_i - \mathcal{C}'_i$, and are sensitive to dipole operators. Importantly, in Λ_c -decays the forward-backward asymmetry $A_{\text{FB}} \propto K_{1c} \propto \mathcal{C}_{10}$ is a clean null test of the SM.

For the phenomenological analysis it is useful to define binned observables

$$\begin{aligned} \mathcal{B}_{[q_{\min}^2, q_{\max}^2]} &= \tau_{\Lambda_c} \int_{q_{\min}^2}^{q_{\max}^2} (2K_{1ss}(q^2) + K_{1cc}(q^2)) dq^2 , \\ \langle A_{\text{FB}} \rangle_{[q_{\min}^2, q_{\max}^2]} &= \frac{3}{2} \frac{\int_{q_{\min}^2}^{q_{\max}^2} K_{1c}(q^2) dq^2}{\int_{q_{\min}^2}^{q_{\max}^2} (2K_{1ss}(q^2) + K_{1cc}(q^2)) dq^2} , \\ \langle F_L \rangle_{[q_{\min}^2, q_{\max}^2]} &= \frac{\int_{q_{\min}^2}^{q_{\max}^2} (2K_{1ss}(q^2) - K_{1cc}(q^2)) dq^2}{\int_{q_{\min}^2}^{q_{\max}^2} (2K_{1ss}(q^2) + K_{1cc}(q^2)) dq^2} , \end{aligned} \quad (3.17)$$

where τ_{Λ_c} denotes the lifetime of the Λ_c -baryon. Note, $0 \leq \langle F_L \rangle_{[q_{\min}^2, q_{\max}^2]} \leq 1$.

bin	q^2 / GeV^2 region	$\mathcal{B}_{\text{exp,bin}}$	$\mathcal{B}_{\text{SM,bin}}$	$\langle F_L \rangle_{\text{SM,bin}}$
low- q^2	[0.045, 0.258]	$< 0.93 \times 10^{-8}$	$[0.26, 0.83] \times 10^{-8}$	[0.62, 0.71]
high- q^2	[1.122, 1.817]	$< 3.0 \times 10^{-8}$	$[0.02, 2.3] \times 10^{-8}$	[0.00, 0.91]
low & high- q^2	[0.045, 0.258] \cup [1.122, 1.817]	$< 2.9 \times 10^{-8}$	$[0.3, 3.1] \times 10^{-8}$	[0.48, 0.71]
ω	[0.552, 0.677]	$(7.3 \pm 2.9) \times 10^{-8}$ †	$[5.1, 9.6] \times 10^{-8}$	[0.57, 0.67]
ρ	[0.346, 0.552] \cup [0.677, 0.932]	$(6.9 \pm 2.0) \times 10^{-8}$ †	$[4.3, 11.9] \times 10^{-8}$	[0.59, 0.66]
ϕ	[0.959, 1.122]	$(3.02 \pm 0.45) \times 10^{-7}$ †	$[2.3, 3.7] \times 10^{-7}$	[0.48, 0.53]
full- q^2	$[4m_\mu^2, (m_{\Lambda_c} - m_p)^2]$	-	$[3.6, 6.0] \times 10^{-7}$	[0.51, 0.57]

Table 1: Experimental 90% C.L. upper limits on the $\Lambda_c \rightarrow p \mu^+ \mu^-$ branching fraction for different q^2 bins [13]. We further provide SM predictions for branching ratios and the longitudinal polarization fraction $\langle F_L \rangle_{\text{bin}}$. † Values extracted from Eq. (3.20).

In the presence of CP-violation the decays of Λ_c and $\bar{\Lambda}_c$ differ. Observables for the conjugated mode $\bar{\Lambda}_c \rightarrow \bar{p} \mu^+ \mu^-$ are denoted by a bar. They can be constructed from the CP-conjugate angular distribution $d^2\bar{\Gamma}/dq^2 d\cos\theta_\ell = \frac{3}{2} (\bar{K}_{1ss} \sin^2\theta_\ell + \bar{K}_{1cc} \cos^2\theta_\ell - \bar{K}_{1c} \cos\theta_\ell)$, where the $\bar{K}_{1ss}, \bar{K}_{1cc}, \bar{K}_{1c}$ are obtained from the K_{1ss}, K_{1cc}, K_{1c} by conjugating the weak phases, respectively. As we keep the definition of θ_ℓ with its reference to the ℓ^+ for the decay and its conjugate identical, there is a minus sign in front of the $\cos\theta_\ell$ -term. This gives, for instance, the forward-backward asymmetry of $\bar{\Lambda}_c \rightarrow \bar{p} \mu^+ \mu^-$ decays as

$$\langle \bar{A}_{\text{FB}} \rangle_{[q_{\text{min}}^2, q_{\text{max}}^2]} = -\frac{3}{2} \frac{\int_{q_{\text{min}}^2}^{q_{\text{max}}^2} \bar{K}_{1c}(q^2) dq^2}{\int_{q_{\text{min}}^2}^{q_{\text{max}}^2} (2\bar{K}_{1ss}(q^2) + \bar{K}_{1cc}(q^2)) dq^2}. \quad (3.18)$$

3.2.1 Modelling resonances

To model the resonance contributions $\Lambda_c \rightarrow pR(\rightarrow \mu^+ \mu^-)$, $R = \rho, \omega, \phi$, we employ a phenomenological ansatz

$$C_9^R(q^2) = \frac{a_\rho e^{i\delta_\rho}}{q^2 - m_\rho^2 + i m_\rho \Gamma_\rho} + \frac{a_\omega e^{i\delta_\omega}}{q^2 - m_\omega^2 + i m_\omega \Gamma_\omega} + \frac{a_\phi e^{i\delta_\phi}}{q^2 - m_\phi^2 + i m_\phi \Gamma_\phi}, \quad (3.19)$$

with the resonance masses m_R and decay widths Γ_R , which we take from Ref. [34], and the a priori unknown strong phases δ_R . The modulus of the resonance parameters a_R are

determined using data from LHCb [13]

$$\begin{aligned}\frac{\mathcal{B}(\Lambda_c^+ \rightarrow p \mu^+ \mu^-)_{\omega\text{-region}}}{\mathcal{B}(\Lambda_c^+ \rightarrow p \mu^+ \mu^-)_{\phi\text{-region}}} &= 0.240 \pm 0.035, \\ \frac{\mathcal{B}(\Lambda_c^+ \rightarrow p \mu^+ \mu^-)_{\rho\text{-region}}}{\mathcal{B}(\Lambda_c^+ \rightarrow p \mu^+ \mu^-)_{\phi\text{-region}}} &= 0.229 \pm 0.056,\end{aligned}\quad (3.20)$$

with the q^2 -regions specified in Table 1 and assuming uncorrelated statistical and systematic uncertainties. We obtain

$$a_\phi = 0.108_{-0.008}^{+0.008} \text{ GeV}^2, \quad a_\omega = 0.074_{-0.015}^{+0.012} \text{ GeV}^2, \quad a_\rho = 0.50_{-0.06}^{+0.06} \text{ GeV}^2, \quad (3.21)$$

where we used the narrow-width approximation for $\mathcal{B}(\Lambda_c^+ \rightarrow p \mu^+ \mu^-)_{\phi\text{-region}} \approx \mathcal{B}(\Lambda_c^+ \rightarrow p \phi) \times \mathcal{B}(\phi \rightarrow \mu^+ \mu^-) = (3.02 \pm 0.45) \times 10^{-7}$ [34]. In the isospin limit $a_\rho/a_\omega = 3$ and $\delta_\rho - \delta_\omega = \pi$, as used in [26]. The ratio $a_\rho/a_\omega = 6.8_{-1.6}^{+2.7}$ obtained from the fit therefore mildly hints at isospin violation in this decay. Here, we used $\delta_\omega - \delta_\rho = \pi$ and $\delta_\phi - \delta_\rho = 0$, but note that other choices for the strong phases give values that agree within uncertainties.

The η and η' are very narrow and less pronounced than the vector meson resonances in the dilepton mass distributions, see [8, 35] for study in $D \rightarrow \pi \ell^+ \ell^-$ decays. This is consistent with the observed hierarchy of the Λ_c -branching ratios $\frac{\mathcal{B}(\Lambda_c^+ \rightarrow p \mu^+ \mu^-)_{\eta\text{-region}}}{\mathcal{B}(\Lambda_c^+ \rightarrow p \mu^+ \mu^-)_{\phi\text{-region}}} = 0.032 \pm 0.014$ [13]. We therefore refrain in this study from including the pseudoscalar resonances in our model, noting that also in the future their use for resonance enhanced new physics signals would require very precise q^2 -binning.

The relative strong phases $\delta_\omega - \delta_\rho$ and $\delta_\phi - \delta_\rho$ cannot be determined from the fit, because the given q^2 regions depend only mildly on the strong phases and hence a fit is not possible with the current precision and binning. Additional bins in regions, where resonances overlap, could pin down these phases in the future. In Fig. 1 we show the $\Lambda_c \rightarrow p \mu^+ \mu^-$ differential branching ratio, including curves (black) with fixed relative strong phases $\delta_{\omega(\phi)} - \delta_\rho$. We learn that the sensitivity is large in the high- q^2 region, however, rates are small. At low q^2 , on the other hand, rates are large but the variation with phases is smaller. In between the ρ/ω and ϕ resonances the impact of the relative strong phases is also significant, and invites further study.

In Tab. 1 we present the SM predictions and data [13] for the branching ratio \mathcal{B}_{SM} , as well as $\langle F_L \rangle_{\text{SM}}$, for different q^2 bins for $\Lambda_c \rightarrow p \mu^+ \mu^-$ decays. The SM uncertainties are predominantly driven by the strong phases and cancel partially in $\langle F_L \rangle$.

The forward-backward asymmetry vanishes in the SM because it is proportional to the product $\mathcal{C}_9^R \mathcal{C}_{10}$. Consequently, even a small NP contribution from \mathcal{C}_{10} can be significantly enhanced through interference with a resonance contribution \mathcal{C}_9^R . We analyze the NP reach and prospects of A_{FB} in Sec. 6.1. For further details, see Ref. [26].

3.2.2 Limits on NP

Using the upper 90% C.L. limits on the branching fractions of $\Lambda_c \rightarrow p \mu^+ \mu^-$ in the low- q^2 region, the high- q^2 region, and the combined region [13] given in Tab. 1, and the resonance parameters given in Eq. (3.21), we obtain the following constraints on the Wilson

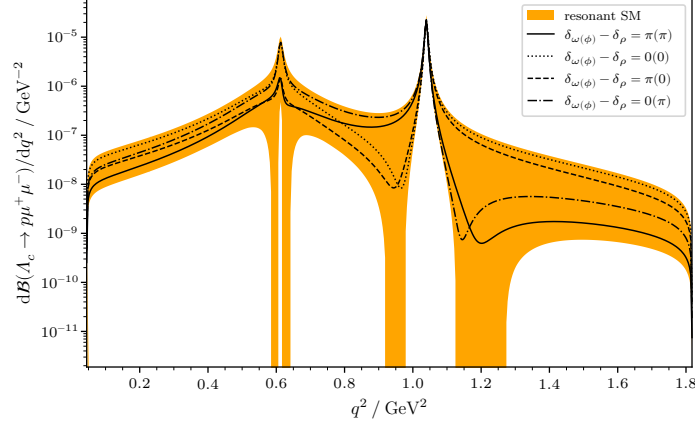


Figure 1: The differential branching ratio of $\Lambda_c \rightarrow p\mu^+\mu^-$ decays including uncertainties predominantly caused by strong phases (orange band). The black curves correspond to different relative strong phases $\delta_\omega - \delta_\rho$ and $\delta_\phi - \delta_\rho$ and illustrate the sensitivity to them in the different q^2 -regions.

coefficients in the low q^2 region

$$\begin{aligned}
& 0.28 + 0.27 |\mathcal{C}_{10} - \mathcal{C}'_{10}|^2 + 0.31 |\mathcal{C}_{10} + \mathcal{C}'_{10}|^2 + 18 |\mathcal{C}_7 - \mathcal{C}'_7|^2 \\
& + 17 |\mathcal{C}_7 + \mathcal{C}'_7|^2 + 0.29 |\mathcal{C}_9 - \mathcal{C}'_9|^2 + 0.31 |\mathcal{C}_9 + \mathcal{C}'_9|^2 \\
& + 1.8 \text{Re} [(\mathcal{C}_7 + \mathcal{C}'_7)(\mathcal{C}_9 + \mathcal{C}'_9)^*] + 2.4 \text{Re} [(\mathcal{C}_7 - \mathcal{C}'_7)(\mathcal{C}_9 - \mathcal{C}'_9)^*] \\
& - 0.23 \text{Re} [\mathcal{C}_9 - \mathcal{C}'_9] - 0.06 \text{Im} [\mathcal{C}_9 - \mathcal{C}'_9] - 0.25 \text{Re} [\mathcal{C}_9 + \mathcal{C}'_9] - 0.07 \text{Im} [\mathcal{C}_9 + \mathcal{C}'_9] \\
& - 0.7 \text{Re} [\mathcal{C}_7 + \mathcal{C}'_7] - 0.20 \text{Im} [\mathcal{C}_7 + \mathcal{C}'_7] - 0.9 \text{Re} [\mathcal{C}_7 - \mathcal{C}'_7] - 0.26 \text{Im} [\mathcal{C}_7 - \mathcal{C}'_7] \lesssim 1,
\end{aligned} \tag{3.22}$$

in the high q^2 region

$$\begin{aligned}
& 0.5 |\mathcal{C}_{10} - \mathcal{C}'_{10}|^2 + 0.15 |\mathcal{C}_{10} + \mathcal{C}'_{10}|^2 + 1.9 |\mathcal{C}_7 - \mathcal{C}'_7|^2 \\
& + 0.6 |\mathcal{C}_7 + \mathcal{C}'_7|^2 + 0.5 |\mathcal{C}_9 - \mathcal{C}'_9|^2 + 0.14 |\mathcal{C}_9 + \mathcal{C}'_9|^2 \\
& + 0.5 \text{Re} [(\mathcal{C}_7 + \mathcal{C}'_7)(\mathcal{C}_9 + \mathcal{C}'_9)^*] + 1.9 \text{Re} [(\mathcal{C}_7 - \mathcal{C}'_7)(\mathcal{C}_9 - \mathcal{C}'_9)^*] \\
& + 0.5 \text{Re} [\mathcal{C}_9 - \mathcal{C}'_9] - 0.04 \text{Im} [\mathcal{C}_9 - \mathcal{C}'_9] + 0.19 \text{Re} [\mathcal{C}_9 + \mathcal{C}'_9] - 0.016 \text{Im} [\mathcal{C}_9 + \mathcal{C}'_9] \\
& + 0.4 \text{Re} [\mathcal{C}_7 + \mathcal{C}'_7] - 0.030 \text{Im} [\mathcal{C}_7 + \mathcal{C}'_7] + 1.0 \text{Re} [\mathcal{C}_7 - \mathcal{C}'_7] - 0.09 \text{Im} [\mathcal{C}_7 - \mathcal{C}'_7] \lesssim 1,
\end{aligned} \tag{3.23}$$

and for the combined region:

$$\begin{aligned}
& 0.10 + 0.6 |\mathcal{C}_{10} - \mathcal{C}'_{10}|^2 + 0.25 |\mathcal{C}_{10} + \mathcal{C}'_{10}|^2 + 8 |\mathcal{C}_7 - \mathcal{C}'_7|^2 \\
& + 6 |\mathcal{C}_7 + \mathcal{C}'_7|^2 + 0.6 |\mathcal{C}_9 - \mathcal{C}'_9|^2 + 0.25 |\mathcal{C}_9 + \mathcal{C}'_9|^2 \\
& + 1.1 \text{Re} [(\mathcal{C}_7 + \mathcal{C}'_7)(\mathcal{C}_9 + \mathcal{C}'_9)^*] + 2.7 \text{Re} [(\mathcal{C}_7 - \mathcal{C}'_7)(\mathcal{C}_9 - \mathcal{C}'_9)^*] \\
& + 0.5 \text{Re} [\mathcal{C}_9 - \mathcal{C}'_9] - 0.06 \text{Im} [\mathcal{C}_9 - \mathcal{C}'_9] + 0.11 \text{Re} [\mathcal{C}_9 + \mathcal{C}'_9] - 0.04 \text{Im} [\mathcal{C}_9 + \mathcal{C}'_9] \\
& + 0.13 \text{Re} [\mathcal{C}_7 + \mathcal{C}'_7] - 0.10 \text{Im} [\mathcal{C}_7 + \mathcal{C}'_7] + 0.8 \text{Re} [\mathcal{C}_7 - \mathcal{C}'_7] - 0.17 \text{Im} [\mathcal{C}_7 - \mathcal{C}'_7] \lesssim 1.
\end{aligned} \tag{3.24}$$

The strongest constraints on $\mathcal{C}_{9,10}$ are from the joint region, whereas those on the dipole operator are from the low q^2 region. Comparison with the constraints from $D \rightarrow \pi\mu^+\mu^-$

and $D \rightarrow \mu^+\mu^-$, given in Eqs. (3.5) and (3.8), shows that the limits from $\Lambda_c \rightarrow p\mu^+\mu^-$ decays are generally weaker. On the other hand, the baryonic decay is sensitive at low q^2 to the photon pole via $\Lambda_c \rightarrow p\gamma^*$, yielding constraints from (3.22) on the electromagnetic dipole operators $\mathcal{O}_7^{(\prime)}$ as

$$|\mathcal{C}_7|, |\mathcal{C}'_7| \lesssim 0.2, \quad (3.25)$$

which are stronger than the ones from radiative decay $D^0 \rightarrow \rho^0\gamma$, $|\mathcal{C}_7^{(\prime)}| \lesssim 0.3$ [9].

Combining data on the branching ratios of $D \rightarrow \pi\mu^+\mu^-$ (3.5) and Λ_c decays (3.24) allows one to constrain \mathcal{C}_9 and \mathcal{C}'_9 individually as

$$|\mathcal{C}_9|, |\mathcal{C}'_9| \lesssim 1.1, \quad (3.26)$$

assuming that no other NP coefficients are present.

At low q^2 and therefore also in the combined region the SM contributions are not entirely negligible compared to the experimental limits. We therefore indicate them by the constant terms on the left hand sides of (3.22) and (3.24), noting that they have larger uncertainties than the NP terms. The finite SM branching ratios tighten the constraints on NP, however, this is within the accuracy of the limits (3.25), (3.26).

The difference in constraints from (3.22) and (3.23) highlight the importance of q^2 -binning. We discuss this in detail for the null test observable A_{FB} in Sec. 6.1, where we study the future NP potential of $\Lambda_c \rightarrow p\ell^+\ell^-$ decays.

3.3 $D \rightarrow P_1 P_2 \ell^+ \ell^-$

We discuss observables of the 4-body decay $D \rightarrow P_1 P_2 \ell^+ \ell^-$. In Sec. 3.3.1 we give the full angular distribution and detail its SM predictions. CP-symmetries and asymmetries of the angular coefficients are discussed in Sec. 3.3.2.

3.3.1 Full angular distribution

The 5-differential decay distribution of $D \rightarrow P_1 P_2 \ell^+ \ell^-$ can be written as

$$\frac{d^5\Gamma}{dq^2 dp^2 d\cos\theta_{P_1} d\cos\theta_\ell d\phi} = \frac{1}{2\pi} \sum_{i=1}^9 c_i(\theta_\ell, \phi) I_i(q^2, p^2, \cos\theta_{P_1}), \quad (3.27)$$

where π^+ equals P_1 in $D \rightarrow \pi^+\pi^-\mu^+\mu^-$ decays, and q^2 and p^2 represent the invariant mass-squared of the dilepton and the $(P_1 P_2)$ -subsystem, respectively. θ_ℓ , θ_{P_1} , and ϕ are the angular variables defined in Ref. [9]. θ_ℓ denotes the angle between the ℓ^- -momentum and the D -momentum in the dilepton center-of-mass system (cms), while θ_{P_1} represents the angle between the P_1 -momentum and the negative direction of flight of the D -meson in the $(P_1 P_2)$ -cms.² The definition of the angles is identical for D and CP-conjugated \bar{D}

²The relation between ϕ and the angle ϕ_{LHCb} used in the experimental analysis [36] by the LHCb collaboration is $\phi = \pi + \phi_{\text{LHCb}}$. Therefore, $I_{4,5,7,8} = -I_{4,5,7,8}^{\text{LHCb}}$.

decays. Specifically, also in $\bar{D} \rightarrow \pi^+ \pi^- \mu^+ \mu^-$ decays $\pi^+ = P_1$. The kinematically accessible phase space is given by

$$4m_\ell^2 < q^2 \leq (m_D - m_{P_1} - m_{P_2})^2, \quad (m_{P_1} + m_{P_2})^2 < p^2 \leq (m_D - \sqrt{q^2})^2, \\ -1 < \cos \theta_{P_1} \leq 1, \quad -1 < \cos \theta_\ell \leq 1, \quad 0 < \phi \leq 2\pi. \quad (3.28)$$

The functions $c_i(\theta_\ell, \phi)$ encode the dependence on the angles θ_ℓ and ϕ

$$c_1 = 1, \quad c_2 = \cos 2\theta_\ell, \quad c_3 = \sin^2 \theta_\ell \cos 2\phi, \quad c_4 = \sin 2\theta_\ell \cos \phi, \quad c_5 = \sin \theta_\ell \cos \phi, \\ c_6 = \cos \theta_\ell, \quad c_7 = \sin \theta_\ell \sin \phi, \quad c_8 = \sin 2\theta_\ell \sin \phi, \quad c_9 = \sin^2 \theta_\ell \sin 2\phi, \quad (3.29)$$

while the angular coefficients $I_i \equiv I_i(q^2, p^2, \cos \theta_{P_1})$ are functions of q^2 , p^2 , and θ_{P_1} . The angular coefficients can be expressed in terms of transversity amplitudes, $H_x^{L,R}$, $x = \perp, \parallel, 0$ [9] as

$$I_1 = \frac{1}{16} \left[|H_0^L|^2 + (L \rightarrow R) + \frac{3}{2} \sin^2 \theta_{P_1} \left\{ |H_\perp^L|^2 + |H_\parallel^L|^2 + (L \rightarrow R) \right\} \right], \\ I_2 = -\frac{1}{16} \left[|H_0^L|^2 + (L \rightarrow R) - \frac{1}{2} \sin^2 \theta_{P_1} \left\{ |H_\perp^L|^2 + |H_\parallel^L|^2 + (L \rightarrow R) \right\} \right], \\ I_3 = \frac{1}{16} \left[|H_\perp^L|^2 - |H_\parallel^L|^2 + (L \rightarrow R) \right] \sin^2 \theta_{P_1}, \\ I_4 = -\frac{1}{8} \left[\text{Re} \left[H_0^L H_\parallel^{L*} \right] + (L \rightarrow R) \right] \sin \theta_{P_1}, \\ I_5 = -\frac{1}{4} \left[\text{Re} \left[H_0^L H_\perp^{L*} \right] - (L \rightarrow R) \right] \sin \theta_{P_1}, \\ I_6 = \frac{1}{4} \left[\text{Re} \left[H_\parallel^L H_\perp^{L*} \right] - (L \rightarrow R) \right] \sin^2 \theta_{P_1}, \\ I_7 = -\frac{1}{4} \left[\text{Im} \left[H_0^L H_\parallel^{L*} \right] - (L \rightarrow R) \right] \sin \theta_{P_1}, \\ I_8 = -\frac{1}{8} \left[\text{Im} \left[H_0^L H_\perp^{L*} \right] + (L \rightarrow R) \right] \sin \theta_{P_1}, \\ I_9 = \frac{1}{8} \left[\text{Im} \left[H_\parallel^{L*} H_\perp^L \right] + (L \rightarrow R) \right] \sin^2 \theta_{P_1}, \quad (3.30)$$

where tensor and (pseudo)-scalar operators are not included, and the lepton mass is neglected. The subscripts 0, \parallel , and \perp represent longitudinal, parallel, and perpendicular polarizations, respectively. Additionally, L and R denote the chirality of the lepton current. By examining the relative signs between the left-handed and right-handed contributions in Eq. (3.30), it follows that finite $I_{5,6,7}$ require non-vanishing axial-vector contributions. These are induced by $\mathcal{O}_{10}^{(\prime)}$, or at higher order from electromagnetic loops, and are very small, hence $I_{5,6,7}$ serve as clean null tests of the SM [9]. The transversity amplitudes can

be written, for the non-resonant part to lowest order in $1/m_c$ [37], as

$$\begin{aligned}
H_i^{L/R} &= \mathcal{C}_-^{L/R}(q^2) \mathcal{F}_i(q^2, p^2, \theta_{P_1}) + \sum_{J=S, P, D, \dots} \mathcal{C}_9^{\mathcal{R}, J}(q^2) \mathcal{F}_{i, J}^{\text{res}}(q^2, p^2, \theta_{P_1}), \quad i = 0, \parallel, \\
H_\perp^{L/R} &= \mathcal{C}_+^{L/R}(q^2) \mathcal{F}_\perp(q^2, p^2, \theta_{P_1}) + \sum_{J=S, P, D, \dots} \mathcal{C}_9^{\mathcal{R}, J}(q^2) \mathcal{F}_{\perp, J}^{\text{res}}(q^2, p^2, \theta_{P_1}),
\end{aligned} \tag{3.31}$$

where

$$\begin{aligned}
\mathcal{C}_\pm^L(q^2) &= \mathcal{C}_9^{\text{eff}}(q^2) + \mathcal{C}_9 \pm \mathcal{C}'_9 - (\mathcal{C}_{10} \pm \mathcal{C}'_{10}) + \kappa \frac{2m_c m_D}{q^2} (\mathcal{C}_7 \pm \mathcal{C}'_7), \\
\mathcal{C}_\pm^R(q^2) &= \mathcal{C}_9^{\text{eff}}(q^2) + \mathcal{C}_9 \pm \mathcal{C}'_9 + \mathcal{C}_{10} \pm \mathcal{C}'_{10} + \kappa \frac{2m_c m_D}{q^2} (\mathcal{C}_7 \pm \mathcal{C}'_7),
\end{aligned} \tag{3.32}$$

with $\kappa = 1 - 2\alpha_s/(3\pi) \ln(\mu/m_c)$ [9], and

$$\mathcal{C}_9^{\mathcal{R}, J}(q^2) = \frac{a_{J, \rho} e^{i\delta_{J, \rho}}}{q^2 - m_\rho^2 + i m_\rho \Gamma_\rho} + \frac{a_{J, \omega} e^{i\delta_{J, \omega}}}{q^2 - m_\omega^2 + i m_\omega \Gamma_\omega} + \frac{a_{J, \phi} e^{i\delta_{J, \phi}}}{q^2 - m_\phi^2 + i m_\phi \Gamma_\phi}. \tag{3.33}$$

This phenomenological ansatz is identical to (3.19) with resonance parameters $a_{J, \mathcal{R}}$, $\delta_{J, \mathcal{R}}$ taking on different values for different decay modes. The additional index J for $D^0 \rightarrow \pi^+ \pi^- \mu^+ \mu^-$ decays is needed to take into account resonances in p^2 with spin $J = 0, 1, \dots$ that decay to $\pi^+ \pi^-$. The parameters $a_{J, \mathcal{R}}$ and phases $\delta_{J, \mathcal{R}}$ are extracted in Sec. 4.1 from a fit to data on the q^2 and p^2 differential distributions of $D^0 \rightarrow \pi^+ \pi^- \mu^+ \mu^-$ from the LHCb collaboration [36]. The resonance coefficient $\mathcal{C}_9^{\mathcal{R}, J}$ does not depend on the transversity, an assumption which can be investigated further using data on hadronic D -decays with polarization information. The functions \mathcal{F}_i and $\mathcal{F}_{i, J}^{\text{res}}$ with $i = 0, \parallel, \perp$ represent the transversity form factors for non-resonant and resonant contributions, respectively, with details provided in Appendix A. Requisite $D \rightarrow \pi\pi$ transition form factors are available only from heavy-hadron chiral perturbation theory [38], subject to large uncertainties. Improved computations from other non-perturbative means would be desirable. Explicit expressions of the I_{1-9} using the transversity amplitudes in Eq. (3.31) are given in App. B.

Due to the smallness of the short-distance contributions in $c \rightarrow u \ell^+ \ell^-$ in the SM, as reviewed in Sec. 2, the decay rate and angular observables of $D \rightarrow P_1 P_2 \ell^+ \ell^-$ decays are

primarily induced by the resonances, that is $\mathcal{C}_9^{\mathcal{R},J}(q^2)$, as

$$\begin{aligned}
I_1^{\text{SM}} &\simeq +\frac{1}{8} \left| \mathcal{C}_9^{\mathcal{R},S} \right|^2 |\mathcal{F}_{0,S}^{\text{res}}|^2 + \left| \mathcal{C}_9^{\mathcal{R},P} \right|^2 \left(\frac{1}{8} |\mathcal{F}_{0,P}^{\text{res}}|^2 + \frac{3}{16} \left(|\mathcal{F}_{\parallel,P}^{\text{res}}|^2 + |\mathcal{F}_{\perp,P}^{\text{res}}|^2 \right) \sin^2 \theta_{P_1} \right) \\
&\quad + \frac{1}{4} \text{Re} \left\{ \mathcal{C}_9^{\mathcal{R},P} \left(\mathcal{C}_9^{\mathcal{R},S} \right)^* \right\} \text{Re}[\mathcal{F}_{0,S}^{\text{res}} \mathcal{F}_{0,P}^{\text{res},*}] + \frac{1}{4} \text{Im} \left\{ \mathcal{C}_9^{\mathcal{R},P} \left(\mathcal{C}_9^{\mathcal{R},S} \right)^* \right\} \text{Im}[\mathcal{F}_{0,S}^{\text{res}} \mathcal{F}_{0,P}^{\text{res},*}], \\
I_2^{\text{SM}} &\simeq -\frac{1}{8} \left| \mathcal{C}_9^{\mathcal{R},S} \right|^2 |\mathcal{F}_{0,S}^{\text{res}}|^2 + \left| \mathcal{C}_9^{\mathcal{R},P} \right|^2 \left(-\frac{1}{8} |\mathcal{F}_{0,P}^{\text{res}}|^2 + \frac{1}{16} \left(|\mathcal{F}_{\parallel,P}^{\text{res}}|^2 + |\mathcal{F}_{\perp,P}^{\text{res}}|^2 \right) \sin^2 \theta_{P_1} \right) \\
&\quad - \frac{1}{4} \text{Re} \left\{ \mathcal{C}_9^{\mathcal{R},P} \left(\mathcal{C}_9^{\mathcal{R},S} \right)^* \right\} \text{Re}[\mathcal{F}_{0,S}^{\text{res}} \mathcal{F}_{0,P}^{\text{res},*}] - \frac{1}{4} \text{Im} \left\{ \mathcal{C}_9^{\mathcal{R},P} \left(\mathcal{C}_9^{\mathcal{R},S} \right)^* \right\} \text{Im}[\mathcal{F}_{0,S}^{\text{res}} \mathcal{F}_{0,P}^{\text{res},*}], \\
I_3^{\text{SM}} &\simeq -\frac{1}{8} \left| \mathcal{C}_9^{\mathcal{R},P} \right|^2 \left(|\mathcal{F}_{\parallel,P}^{\text{res}}|^2 - |\mathcal{F}_{\perp,P}^{\text{res}}|^2 \right) \sin^2 \theta_{P_1}, \\
I_4^{\text{SM}} &\simeq \left[-\frac{1}{4} \left| \mathcal{C}_9^{\mathcal{R},P} \right|^2 \text{Re}[\mathcal{F}_{0,P}^{\text{res}} \mathcal{F}_{\parallel,P}^{\text{res},*}] \right. \\
&\quad \left. + \frac{1}{4} \text{Im} \left\{ \mathcal{C}_9^{\mathcal{R},P} \left(\mathcal{C}_9^{\mathcal{R},S} \right)^* \right\} \text{Im}[\mathcal{F}_{\parallel,P}^{\text{res}} \mathcal{F}_{0,S}^{\text{res},*}] - \frac{1}{4} \text{Re} \left\{ \mathcal{C}_9^{\mathcal{R},P} \left(\mathcal{C}_9^{\mathcal{R},S} \right)^* \right\} \text{Re}[\mathcal{F}_{0,S}^{\text{res}} \mathcal{F}_{\parallel,P}^{\text{res},*}] \right] \sin \theta_{P_1}, \\
I_8^{\text{SM}} &\simeq \left[+\frac{1}{4} \left| \mathcal{C}_9^{\mathcal{R},P} \right|^2 \text{Im}[\mathcal{F}_{\perp,P}^{\text{res}} \mathcal{F}_{0,P}^{\text{res},*}] \overset{\approx 0}{\cancel{\phantom{\text{Im}[\mathcal{F}_{\perp,P}^{\text{res}} \mathcal{F}_{0,P}^{\text{res},*}]}} \right. \\
&\quad \left. + \frac{1}{4} \text{Re} \left\{ \mathcal{C}_9^{\mathcal{R},P} \left(\mathcal{C}_9^{\mathcal{R},S} \right)^* \right\} \text{Im}[\mathcal{F}_{\perp,P}^{\text{res}} \mathcal{F}_{0,S}^{\text{res},*}] + \frac{1}{4} \text{Im} \left\{ \mathcal{C}_9^{\mathcal{R},P} \left(\mathcal{C}_9^{\mathcal{R},S} \right)^* \right\} \text{Re}[\mathcal{F}_{0,S}^{\text{res}} \mathcal{F}_{\perp,P}^{\text{res},*}] \right] \sin \theta_{P_1}, \\
I_9^{\text{SM}} &\simeq -\frac{1}{4} \left| \mathcal{C}_9^{\mathcal{R},P} \right|^2 \text{Im}[\mathcal{F}_{\parallel,P}^{\text{res}} \mathcal{F}_{\perp,P}^{\text{res},*}] \overset{\approx 0}{\cancel{\phantom{\text{Im}[\mathcal{F}_{\parallel,P}^{\text{res}} \mathcal{F}_{\perp,P}^{\text{res},*}]}} \sin^2 \theta_{P_1}. \tag{3.34}
\end{aligned}$$

Therefore, while $I_{5,6,7}^{\text{SM}} = 0$ due to the GIM-mechanism, $I_{1,2,3,4,8,9}^{\text{SM}}$ are finite. As indicated by the crossed out terms above in Eq. (3.34), the product of P-wave form factors $\mathcal{F}_{i,P}^{\text{res}} \mathcal{F}_{j,P}^{\text{res},*}$ is real assuming universality between different polarizations i, j . In this case I_9^{SM} also vanishes. I_8^{SM} receives contributions from S-P-interference. Its associated angular observable $\langle I_8^{\text{SM}} |_{\text{S-P}} \rangle$, defined in Sec. 3.3.2, vanishes after integration over $\cos \theta_{P_1}$, schematically $\left(\int_0^1 - \int_{-1}^0 \right) I_8^{\text{SM}} |_{\text{S-P}} d\cos \theta_{P_1} = 0$ [39]. On the other hand, the pure P-wave contribution to I_8^{SM} would be finite for non-universal form factors, and does *not* vanish after $\cos \theta_{P_1}$ -integration.

The expressions (3.34) allow to probe the resonance structure and long-distance dynamics underlying $D \rightarrow P_1 P_2 \ell^+ \ell^-$ decays. For instance, I_3^{SM} exclusively captures P-wave contributions, while $I_1^{\text{SM}} + I_2^{\text{SM}}$ eliminates S-wave contributions. The difference $I_1^{\text{SM}} - I_2^{\text{SM}}$ is sensitive to these S-wave contributions, retaining a P-wave contribution and S-P-interference terms. The latter are also present in I_4^{SM} . Details on how the angular observables I_i can be extracted from the 5-differential distribution (3.27) are discussed in Ref. [9]. The distributions including D-waves have been analyzed in [37].

3.3.2 CP-symmetries and asymmetries

We present the angular observables related to the angular coefficients I_i given in Eqs. (B.1)-(B.9). We use the same conventions as LHCb Ref. [36], that is

$$\begin{aligned}\langle S_i \rangle_{[q_{\min}^2, q_{\max}^2]} &= \frac{1}{2} \left[\langle I_i \rangle_{[q_{\min}^2, q_{\max}^2]} + (-) \langle \bar{I}_i \rangle_{[q_{\min}^2, q_{\max}^2]} \right], \\ \langle A_i \rangle_{[q_{\min}^2, q_{\max}^2]} &= \frac{1}{2} \left[\langle I_i \rangle_{[q_{\min}^2, q_{\max}^2]} - (+) \langle \bar{I}_i \rangle_{[q_{\min}^2, q_{\max}^2]} \right],\end{aligned}\quad (3.35)$$

for the CP-even (CP-odd) coefficients $\langle I_{2,3,4,7} \rangle$ ($\langle I_{5,6,8,9} \rangle$), with

$$\begin{aligned}\langle I_{2,3,6,9} \rangle (q^2) &= \frac{1}{\Gamma_{[q_{\min}^2, q_{\max}^2]}} \int_{(m_{P_1} + m_{P_2})^2}^{(m_D - \sqrt{q^2})^2} dp^2 \int_{-1}^1 d \cos \theta_{P_1} I_{2,3,6,9}, \\ \langle I_{4,5,7,8} \rangle (q^2) &= \frac{1}{\Gamma_{[q_{\min}^2, q_{\max}^2]}} \int_{(m_{P_1} + m_{P_2})^2}^{(m_D - \sqrt{q^2})^2} dp^2 \left[\int_0^1 d \cos \theta_{P_1} - \int_{-1}^0 d \cos \theta_{P_1} \right] I_{4,5,7,8},\end{aligned}\quad (3.36)$$

for $q^2 \in [q_{\min}^2, q_{\max}^2]$ and the binned observables

$$\langle I_{2-9} \rangle_{[q_{\min}^2, q_{\max}^2]} = \int_{q_{\min}^2}^{q_{\max}^2} dq^2 \langle I_{2-9} \rangle (q^2). \quad (3.37)$$

The q^2 -binned decay rate $\Gamma_{[q_{\min}^2, q_{\max}^2]}$ is obtained after phase space integration, see Eqs. (3.28), as

$$\Gamma_{[q_{\min}^2, q_{\max}^2]} = \int_{q_{\min}^2}^{q_{\max}^2} dq^2 \int_{(m_{P_1} + m_{P_2})^2}^{(m_D - \sqrt{q^2})^2} dp^2 \int_{-1}^1 d \cos \theta_{P_1} 2 \left(I_1 - \frac{I_2}{3} \right). \quad (3.38)$$

In our analysis we compute the decay rate $\Gamma_{[q_{\min}^2, q_{\max}^2]}$, unless stated otherwise, including NP effects from the Wilson coefficients. While viable NP-effects in the decay rate are too small to be noticeable this enables to take into account correlations in the fit in ratio-type observables such as S_i, A_i in a consistent manner. The $\langle \bar{I}_i \rangle$ in Eq. (3.35) are obtained by conjugating the NP weak phases. In addition also the SM phases in the CKM factors $V_{cd}^* V_{ud}$ and $V_{cs}^* V_{us}$ in the resonance contributions should be conjugated, however, CP-violation is here very small and this has a negligible effect. Therefore, we complex conjugate the NP weak phases, that is, conjugating $\mathcal{C}_{7,9,10}^{(\prime)}$

$$\langle \bar{I}_i \rangle \equiv +(-) \langle I_i (\mathcal{C}_{7,9,10}^{(\prime)*}) \rangle, \quad (3.39)$$

for CP-even (CP-odd) angular coefficients. In the CP-limit holds $\langle S_i \rangle = \langle I_i \rangle$ and $\langle A_i \rangle = 0$.

In Fig. 2, we illustrate the impact of NP in the null test distributions $\langle I_{5,6,7} \rangle (q^2)$,³ as defined in Eqs. (3.36), using the central values of resonance parameters of scenario 4 given in Tab. 2. We employ the same binning as in the LHCb analysis [36]. We display different benchmarks $\mathcal{C}_{10} = 0.5$ (red), $\mathcal{C}'_{10} = 0.5$ (yellow), $\mathcal{C}_{10} = 0.5i$ (blue) and $\mathcal{C}'_{10} = 0.5i$ (green).

³Private communication revealed an error in Fig. 3 of [9]. The square of $m_{P_1}^2$ below Eq. (44) was missing in the numerics of the plots of $I_{5,6,7}$ in [9]. Once this is corrected, the curves change, but remain at the same order of magnitude. We are grateful to Stefan de Boer for correspondence and confirmation.

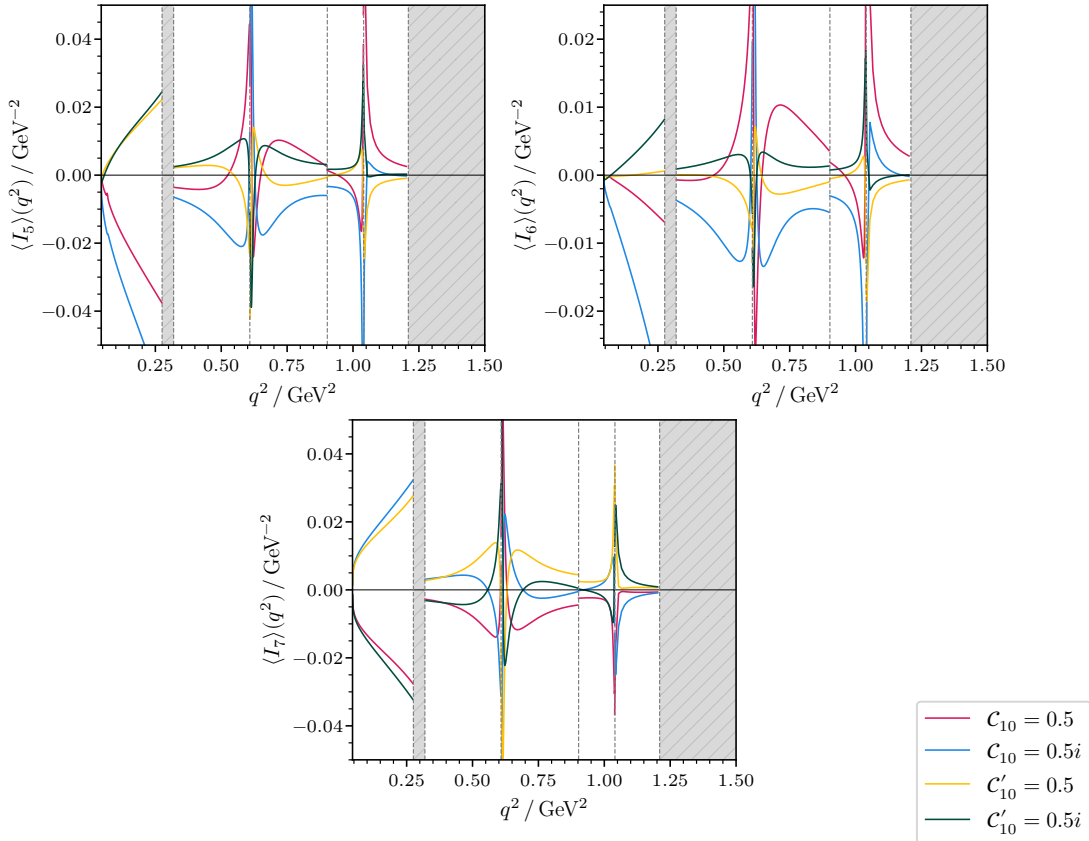


Figure 2: $\langle I_{5,6,7} \rangle(q^2)$ with normalization $\Gamma_{[q_{\min}^2, q_{\max}^2]}$ depending on the q^2 -region and corresponding to the bins, indicated by the gray dashed vertical lines, used by LHCb [36]. NP signals are illustrated with $\mathcal{C}_{10} = 0.5$ (red), $\mathcal{C}'_{10} = 0.5$ (yellow), $\mathcal{C}_{10} = 0.5i$ (blue) and $\mathcal{C}'_{10} = 0.5i$ (green). No data are reported by the experiment in the gray shaded areas.

No data are reported in [36] around the η resonance with $q^2 = m_\eta^2 \sim 0.3 \text{ GeV}^2$ and the high- q^2 endpoint region. The vertical dashed lines denote the boundaries of the bins. The interference between SM resonances and NP contributions gives the largest effects to the null tests $\langle I_{5,6,7} \rangle$ near $q^2 \simeq m_\rho^2$ or m_ϕ^2 .

4 Analysis of $D^0 \rightarrow \pi^+ \pi^- \mu^+ \mu^-$ decays

We present a detailed phenomenological analysis of $D^0 \rightarrow \pi^+ \pi^- \mu^+ \mu^-$ observables. In the appendix in Tab. 6 we give the available measurements in the categories “SM measurements”, with subset “good” bins, which are dominated by SM contributions, and NP measurements, with observables that are negligible in the SM. We use the former to determine resonance parameters in the ansatz (3.33) in Sec. 4.1, and the latter to work out constraints on NP from $D^0 \rightarrow \pi^+ \pi^- \mu^+ \mu^-$ observables in Sec. 4.2. In Sec. 4.3 we discuss contributions beyond the ansatz (3.33) with S- and P-wave $\pi\pi$ -resonances.

4.1 Fitting resonance parameters

To describe the resonant SM contribution, we introduce six magnitude factors $a_{P(S),R}$ and six phases $\delta_{P(S),R}$ in $\mathcal{C}_9^{\mathcal{R},P(S)}$ (see Eq. (3.33)), along with a relative magnitude factor $a_{p^2,\omega}$ and phase $\delta_{p^2,\omega}$ for the P-wave lineshape (see Eq. (A.6)). With available data [36, 40] there is no sensitivity to the relative phase between S- and P-wave contributions, and we set this phase to zero. Observables sensitive to this phase have been discussed in Ref. [39]. In branching ratios, only relative phases between resonances matter. A relative phase between resonant SM and NP only appears via interference terms and cannot be determined through a fit without significant NP in the data. Therefore, in the SM fit, we set $\delta_{S,\phi} = \delta_{P,\phi} = \pi$ and vary the SM-NP strong phase for fits that include NP Wilson coefficients.⁴

We employ the SM measurements listed in Tab. 6, including branching ratios and the angular symmetries $\langle S_{2,3,4} \rangle$. Available data include the differential distributions $d\Gamma/d\sqrt{q^2}$ and $d\Gamma/d\sqrt{p^2}$ [36] which are provided, however, without systematic uncertainties, accounting for unfolded detector effects and bin-to-bin correlations. Given the complexity of disentangling resonances from short-distance NP effects we suggest making this type of information available in the future, in addition to the double differential distribution.

As observed in Ref. [39], using a similar ansatz as Eq. (3.31), the fit to the $D \rightarrow \pi^+\pi^-\mu^+\mu^-$ data [36, 40] is not satisfactory. This complexity, already noted in [39], may arise from missing theoretical descriptions that, if included, could potentially explain the kinematic regions of the data that are not well understood. This concerns in particular the high $\pi\pi$ and the low $\mu\mu$ mass bins, which constitute hence rather “bad” bins. Following a similar approach as Ref. [39], we define “good” bins as those with $\sqrt{q^2} > 0.6 \text{ GeV}$ for $d\Gamma/d\sqrt{q^2}$, $\sqrt{p^2} < 0.9 \text{ GeV}$ for $d\Gamma/d\sqrt{p^2}$, and $\sqrt{q^2} \geq 0.565 \text{ GeV}$ for \mathcal{B} and $\langle S_{2,3,4} \rangle$. Kinematic cuts in both q^2 and p^2 , without having access to the double differential and thus correlations, introduces potentially inconsistencies. We estimate this effect to be small, by comparing the outcome of fits with all SM measurements and just “good” bins, such as scenario 1 and 2 defined below.

We perform fits in scenarios with different resonance models and data sets. Scenario 1,2 and 5 exclude the ω in the P-wave as in [39]. Furthermore, we consider two exploratory scenarios, 9 and 10, where we allow for effective contributions to the matrix element of \mathcal{O}_9 and \mathcal{O}_{10} , denoted by r_9 and r_{10} , respectively. r_9 can be interpreted as a constant SM contribution from the strong interaction to \mathcal{C}_9 , beyond the phenomenological ansatz for \mathcal{C}_9^R . We also consider effective contributions r_{10} to the axial-vector current \mathcal{C}_{10} , to check if this is an artifact of the fit. We analyze the following scenarios:

1. Including all SM measurements and excluding $\omega \rightarrow \ell^+\ell^-$ in P-wave with $a_{P,\omega} = \delta_{P,\omega} = 0$.
2. Including only the “good” bins of all SM measurements and excluding $\omega \rightarrow \ell^+\ell^-$ in P-wave with $a_{P,\omega} = \delta_{P,\omega} = 0$ (same scenario as in Ref. [39]).

⁴The undetermined strong phase affects upper limits, because a single observable $\langle S(A)_j \rangle_{[q_j^2, q_k^2]}$ can vanish even in the presence of large NPs by tuning the overall resonance strong phase. Therefore, multiple measurements with different dependence on this phase are required to improve the NP reach.

3. Including all SM measurements and all parameters.
4. Including only the “good” bins of all SM measurements and all parameters.
5. Including only $\langle S_{2,3,4} \rangle$ & \mathcal{B} measurements and excluding $a_{P,\omega}$, $\delta_{P,\omega}$ and $a_{p^2,\omega}$, $\delta_{p^2,\omega}$.
6. Including only the “good” bins of $\langle S_{2,3,4} \rangle$ & \mathcal{B} measurements, excluding $a_{p^2,\omega}$, $\delta_{p^2,\omega}$ and imposing the isospin relations $a_{P(S),\omega}/a_{P(S),\rho} = 1/3$, $\delta_{P(S),\omega} = \delta_{P(S),\rho} + \pi$.
7. Including only $\langle S_{2,3,4} \rangle$ & \mathcal{B} measurements and excluding $a_{p^2,\omega}$ and $\delta_{p^2,\omega}$.
8. Including only the “good” bins of $\langle S_{2,3,4} \rangle$ & \mathcal{B} measurements and excluding $a_{p^2,\omega}$, $\delta_{p^2,\omega}$.
9. Including all SM measurements and all parameters together with effective contributions r_9, r_{10} to the matrix element of $\mathcal{O}_9, \mathcal{O}_{10}$.
10. Including the “good” bins and all parameters together with r_9, r_{10} .

We perform fits of the resonance parameters for all scenarios using the methodology described in Ref. [41]. Tab. 2 shows the resulting best-fit values and their 1σ uncertainties, together with the reduced chi-square χ^2/dof , the number of observables and the number of fit parameters. The differential $m(\pi^+\pi^-) = \sqrt{p^2}$ and $m(\mu^+\mu^-) = \sqrt{q^2}$ spectra in the scenarios after the fit together with data (black points) are shown in Fig. 3. Our results are consistent with Refs. [9, 39].

fit scenario	1	2	3	4	5	6	7	8	9	10
$a_{P,\rho}/\text{GeV}^2$	$0.270^{+0.019}_{-0.019}$	$0.261^{+0.019}_{-0.019}$	$0.322^{+0.028}_{-0.028}$	$0.289^{+0.029}_{-0.030}$	$0.29^{+0.04}_{-0.05}$	$0.213^{+0.024}_{-0.028}$	$0.32^{+0.05}_{-0.12}$	$0.21^{+0.16}_{-0.26}$	$0.285^{+0.024}_{-0.024}$	$0.264^{+0.024}_{-0.024}$
$a_{P,\omega}/a_{P,\rho}$	0	0	$0.190^{+0.010}_{-0.011}$	$0.199^{+0.014}_{-0.019}$	0	1/3	$0.08^{+0.14}_{-0.10}$	$0.3^{+1.7}_{-0.4}$	$0.198^{+0.014}_{-0.016}$	$0.208^{+0.014}_{-0.019}$
$a_{P,\phi}/a_{P,\rho}$	$0.291^{+0.012}_{-0.012}$	$0.306^{+0.012}_{-0.013}$	$0.217^{+0.020}_{-0.017}$	$0.256^{+0.030}_{-0.024}$	$0.26^{+0.04}_{-0.02}$	$0.37^{+0.05}_{-0.05}$	$0.24^{+0.14}_{-0.03}$	$0.38^{+0.45}_{-0.19}$	$0.252^{+0.018}_{-0.016}$	$0.295^{+0.023}_{-0.019}$
$\delta_{P,\rho}$	$2.67^{+0.18}_{-0.16}$	$2.69^{+0.22}_{-0.18}$	$2.38^{+0.23}_{-0.18}$	$2.34^{+0.32}_{-0.20}$	$3.4^{+1.3}_{-1.5}$	$3.3^{+1.7}_{-2.0}$	$3.4^{+1.4}_{-1.7}$	$2.9^{+1.9}_{-1.9}$	$2.17^{+0.19}_{-0.19}$	$2.12^{+0.22}_{-0.21}$
$\delta_{P,\omega}$	0	0	$5.09^{+0.26}_{-0.24}$	$4.9^{+0.4}_{-0.4}$	0	$\delta_{P,\rho} + \pi$	$5.9^{+2.0}_{-2.0}$	$4.9^{+5.5}_{-5.5}$	$4.81^{+0.28}_{-0.31}$	$4.85^{+0.24}_{-0.24}$
$a_{p^2,\omega}$	$0.0033^{+0.0007}_{-0.0007}$	$0.0036^{+0.0008}_{-0.0008}$	$0.0025^{+0.0007}_{-0.0007}$	$0.0030^{+0.0008}_{-0.0008}$	0	0	0	0	$0.0025^{+0.0007}_{-0.0008}$	$0.0030^{+0.0008}_{-0.0008}$
$\delta_{p^2,\omega}$	$4.62^{+0.27}_{-0.29}$	$4.71^{+0.27}_{-0.30}$	$4.6^{+0.3}_{-0.4}$	$4.7^{+0.3}_{-0.3}$	0	0	0	0	$4.8^{+0.3}_{-0.4}$	$4.9^{+0.3}_{-0.3}$
$a_{S,\rho}/a_{P,\rho}$	$42.5^{+4.4}_{-4.3}$	$43.9^{+4.9}_{-4.7}$	$31.1^{+8.7}_{-9.4}$	$43.2^{+10.7}_{-11.2}$	$47.8^{+14.6}_{-18.3}$	$43.1^{+13.8}_{-13.5}$	$44.9^{+29.4}_{-17.1}$	$63.1^{+293.2}_{-64.0}$	$35.7^{+7.1}_{-6.8}$	$51.3^{+6.5}_{-7.5}$
$a_{S,\omega}/a_{S,\rho}$	$0.271^{+0.023}_{-0.020}$	$0.271^{+0.027}_{-0.022}$	$0.07^{+0.07}_{-0.07}$	$0.07^{+0.07}_{-0.07}$	$0.09^{+0.08}_{-0.10}$	1/3	$0.07^{+0.12}_{-0.12}$	0	$0.10^{+0.07}_{-0.07}$	$0.00^{+0.05}_{-0.00}$
$a_{S,\phi}/a_{S,\rho}$	$0.08^{+0.06}_{-0.08}$	$0.04^{+0.08}_{-0.04}$	$0.31^{+0.14}_{-0.08}$	$0.20^{+0.08}_{-0.06}$	$0.06^{+0.09}_{-0.06}$	$0.00^{+0.26}_{-0.00}$	$0.06^{+0.09}_{-0.06}$	$0.09^{+0.08}_{-0.09}$	$0.24^{+0.07}_{-0.06}$	$0.00^{+0.14}_{-0.00}$
$\delta_{S,\rho}$	$4.14^{+0.18}_{-0.16}$	$4.14^{+0.21}_{-0.19}$	$3.7^{+0.9}_{-1.1}$	$3.5^{+1.3}_{-1.4}$	$1.6^{+3.3}_{-3.3}$	$2.3^{+2.5}_{-2.5}$	$1.6^{+3.3}_{-3.3}$	$0.3^{+2.6}_{-2.6}$	$5.8^{+0.6}_{-0.6}$	$0.4^{+0.5}_{-0.5}$
$\delta_{S,\omega}$	0	0	$1.1^{+1.4}_{-1.4}$	$1.0^{+1.7}_{-1.8}$	$5.6^{+3.6}_{-3.6}$	$\delta_{S,\rho} + \pi$	$5.3^{+3.7}_{-3.7}$	0	$3.4^{+1.1}_{-1.0}$	0
Re r_9	-	-	-	-	-	-	-	-	$2.9^{+0.4}_{-0.4}$	$2.2^{+0.8}_{-1.0}$
Im r_9	-	-	-	-	-	-	-	-	$0.5^{+1.1}_{-1.0}$	$2.2^{+0.9}_{-1.2}$
Re r_{10}	-	-	-	-	-	-	-	-	$0.0^{+0.8}_{-0.8}$	$-0.0^{+0.9}_{-0.9}$
Im r_{10}	-	-	-	-	-	-	-	-	$0.0^{+0.8}_{-0.8}$	$-0.0^{+0.9}_{-0.9}$
χ^2	581.17	288.13	516.54	250.15	66.42	60.93	65.89	49.72	469.20	231.52
# obs.	193	124	193	124	18	17	18	14	193	124
# ang. obs.	3	3	3	3	3	3	3	3	3	3
# ang. bins	5	4	5	4	5	5	5	4	5	4
# $d\Gamma/d\sqrt{q^2}$ bins	85	49	85	49	0	0	0	0	85	49
# $d\Gamma/d\sqrt{p^2}$ bins	92	62	92	62	0	0	0	0	92	62
# \mathcal{B} bins	1	1	1	1	3	2	3	2	1	1
# fit parameters	9	9	12	12	8	6	10	8	16	15
χ^2/dof	3.16	2.51	2.85	2.23	6.64	5.54	8.24	8.29	2.65	2.12

Table 2: Best fit values and uncertainties of the resonance parameters in different fit scenarios detailed in the main text. An exact zero (0) means a parameter is set to zero as an input to the fit. To highlight that the $r_{9,10}$ parameters are only included in scenario 9 and 10 we use a ‘-’ for the other scenarios here.

We observe the following general pattern

$$a_{P,\rho} \simeq 0.3 \text{ GeV}^2, \quad a_{P,\phi}/a_{P,\rho} \simeq 0.3, \quad \delta_{P,\rho} \simeq 3, \quad a_{S,\rho}/a_{P,\rho} \simeq 40, \\ \delta_{P,\omega} \sim 0, \quad \delta_{S,\omega} \sim 0 \text{ (except scenario 9)}, \quad a_{p^2,\omega} \lesssim 0.003, \quad (4.1)$$

where we identify 0 with 2π for phases. The remaining parameters vary between the scenarios. We identify five groups where the best-fit values of resonance parameters are in agreement: scenarios 1 and 2, scenarios 3 and 4, scenarios 5 and 7, scenarios 6 and 8 (with disagreement in S-wave parameters), and scenarios 9 and 10 (with disagreement in $a_{S,\rho}/a_{P,\rho}$).

The ratio $a_{P,\omega}/a_{P,\rho}$ is either set to zero or consistent with zero in scenarios 1, 2, 5, and 7. All other scenarios have $a_{P,\omega}/a_{P,\rho} \sim 0.2 - 0.3$. The value of $a_{S,\omega}$ is only large if we set $a_{P,\omega}$ to zero with the exception of scenario 6 that uses isospin relations. This could be disentangled using the observables proposed in Ref. [39], which are more sensitive to S-wave contributions.

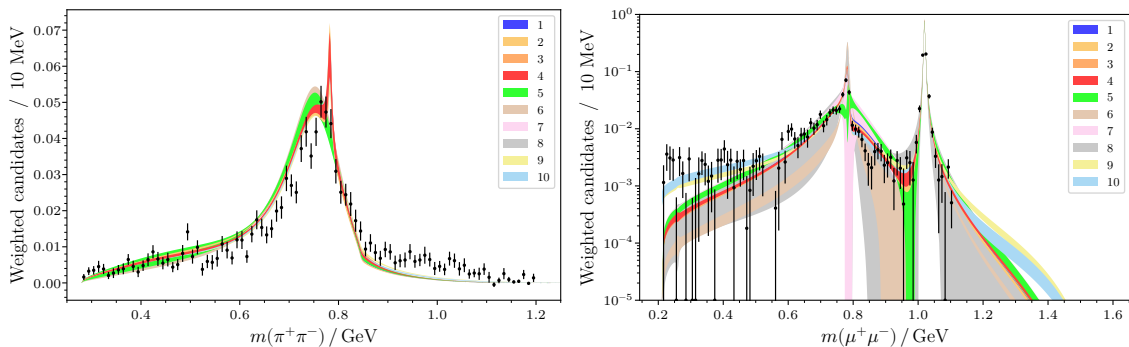


Figure 3: Differential branching fractions for $D \rightarrow \pi^+ \pi^- \mu^+ \mu^-$ decays in invariant masses $m(\pi^+ \pi^-) = \sqrt{p^2}$ (left panel) and $m(\mu^+ \mu^-) = \sqrt{q^2}$ (right panel) for the scenarios detailed in Sec. 4.1. Data points (black) are from LHCb [36].

Scenarios 5,6,7,8, are based on a reduced set of observables, $\langle S_{2,3,4} \rangle$ and \mathcal{B} only, and data are not sufficient to fully determine all resonance parameters. In this case we exclude them from the fit, see Tab. 2. Technically, in the code we set them to zero. These scenarios all have $\chi^2/\text{dof} > 5$, while all other scenarios have $\chi^2/\text{dof} \sim 2 - 3$. This highlights the importance of differential decay distributions for the theoretical modelling.

The best fit for $r_{9,10} = 0$ is obtained in scenario 4, with $\chi^2/\text{dof} = 2.23$, closely followed by 2 and 3. Interestingly, we find that the overall best $\chi^2/\text{dof} = 2.12$ has scenario 10, favoring a large $r_9 \sim 2$ with an order one phase, and vanishing $r_{10} \sim 0$. As large values of NP in $\mathcal{C}_9 \sim 2$ are in tension with limits (3.26) from other $c \rightarrow u \mu^+ \mu^-$ modes, this points to missing hadronic contributions to the operator \mathcal{O}_9 in $D \rightarrow \pi^+ \pi^- \mu^+ \mu^-$. The right panel of Fig. 3 supports also that the presence of $r_9 \sim 2$ in scenario 10 (light blue) and 9 (lemon) improves the agreement with data (black) [36] at low q^2 . Both scenarios 9 and 10 feature also larger high dimuon mass tails, where, however, no data is available and rates decline. Further theoretical investigation is desirable but is beyond the scope of this work.

The CP-averaged angular observables $\langle S_{2,3,4} \rangle$ together with the binned branching ratio using the fit values of the resonance parameters for the different scenarios are displayed in Fig. 4. The predictions of the various scenarios are in part largely overlapping. For the scenarios with lowest χ^2/dof , see Tab. 2, scenario 10 (light blue) is underneath scenario 4 (red), if it is not visible. We consider uncertainties in $D \rightarrow \rho$ and $D \rightarrow f_0(500)$ FFs, the Blatt-Weißkopf factor r_{BW} of the lineshapes, as well as the masses and widths; see Appendix A for details. We observe that the first two low- q^2 bins in $\langle S_2 \rangle$ and $\langle S_4 \rangle$ as well as the low- q^2 bin of \mathcal{B} are in tension with the data. For this reason, we only consider the other bins with higher dilepton mass in the global fits to $\mathcal{C}_{7,9,10}^{(\prime)}$. Moreover, our framework predicts $\langle S_9^{\text{SM}} \rangle = 0$,⁵ while LHCb finds deviations from zero for some of the high- q^2 bins with the largest value being $\langle S_9 \rangle = (16.9 \pm 4.4)\%$ for $[0.950-1.02]$ GeV [36], a local anomaly of 3.8σ . A NP explanation would require large values of $\mathcal{C}_9^{(\prime)}$, which are already excluded (3.26). Therefore we do not take data on $\langle S_9 \rangle$ into account as this would just add a constant to the χ^2 -function.

Since we use “good” bins only and here the exploratory scenario 10 is very much in agreement with scenario 4, we use the latter and its best-fit values of hadronic parameters for $D \rightarrow \pi^+\pi^-\mu^+\mu^-$ decays in the global fit worked out in Sec. 5. All best-fit values of hadronic parameters in scenario 4 and 10 (except r_9) agree within $\sim 1\sigma$.

4.2 Fits to NP in different scenarios

We perform global fits to NP driven by $\mathcal{C}_{7,9,10}$ in the various model scenarios defined in Sec. 4.1. We set the resonance parameters to the best-fit values given in Tab. 2. The experimental data included in NP fits cover the remaining angular observables not considered in the resonance fit, that is, the NP measurements in Tab. 6. In each fit scenario, we only include those observables that depend on the fit parameters. For $\mathcal{C}_{7,9}$, we include $\langle S_8 \rangle$ and $\langle A_{2,3,4,8,9} \rangle$, excluding the two lowest q^2 -bins, which we are unable to explain for the observables $\langle S_{2,4} \rangle$, see Fig. 4. Likewise, for \mathcal{C}_{10} , we include $\langle S_{5,6,7} \rangle$ and $\langle A_{5,6,7} \rangle$ in the same q^2 -bins. To fit the ratio-type observables we also take data on the differential branching ratios into account. We further include $\langle S_{2,3,4} \rangle$ in additional fits for $\mathcal{C}_{7,9,10}$. Using branching ratios or $\langle S_{2,3,4} \rangle$ in the resonance *and* the NP fit may introduce inconsistencies due to potential double counting. A more consistent approach would be to simultaneously fit all parameters, including both resonance and NP contributions. However, with present data this approach is not feasible. As $\langle S_{2,3,4} \rangle$ only slightly improves the fit, we do not use these observables for global fits worked out in Sec. 5.

The results, shown in Fig. 5, indicate that the bounds on $\mathcal{C}_{7,9}$ are very sensitive to the assumptions regarding the extraction of resonance parameters, whereas the bounds on \mathcal{C}_{10} are rather stable over the model scenarios. Comparing scenario 4 (red) with the exploratory scenario 10 (light blue) we learn that the latter is significantly more constraining in $\mathcal{C}_{7,9}$ fits. Overall, the limits from $D \rightarrow \pi^+\pi^-\mu^+\mu^-$ are much weaker than from 2- and 3-body decays obtained in Secs. 3.1 and 3.2. Therefore, we expect that present $D \rightarrow \pi^+\pi^-\mu^+\mu^-$ data have only a minor impact on the global $|\Delta c| = |\Delta u| = 1$ fits performed in Sec. 5.

⁵This can be lifted with transversity-dependence, see (3.34).

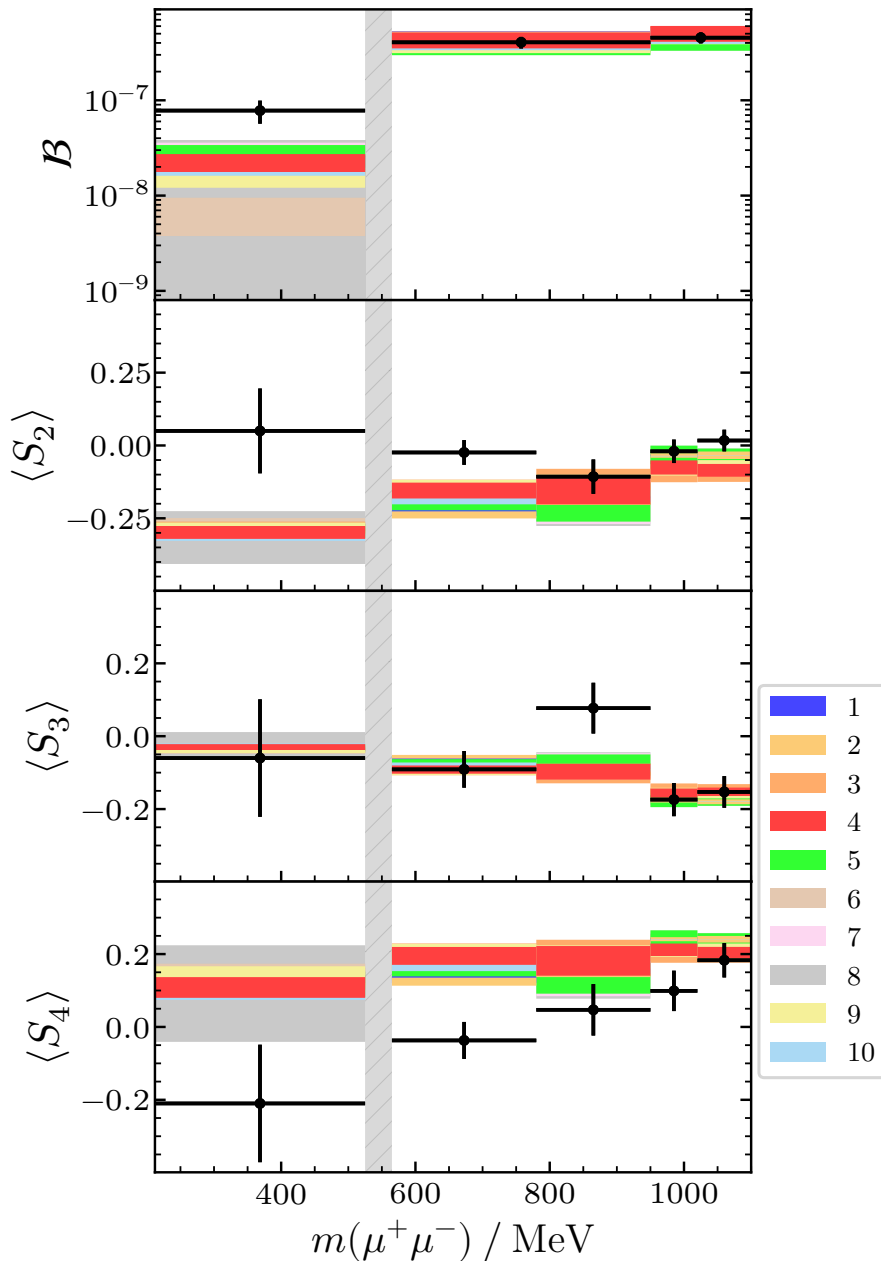


Figure 4: Data (black) on the $D \rightarrow \pi^+\pi^-\mu^+\mu^-$ binned branching ratio [40] and CP-averaged observables $\langle S_{2,3,4} \rangle$ [36] and SM predictions using the best-fit values of the resonance parameters for the different scenarios. Scenarios largely overlap. For the ones with lowest χ^2/dof , scenario 10 (light blue) is in part underneath scenario 4 (red), see text. Note, $\langle S_4 \rangle = -\langle S_4^{\text{LHCb}} \rangle$, see footnote 2.

The reason for the comparatively weak bounds despite existing advanced measurements are twofold: Firstly, the experimental sensitivity [36] is not quite at the level where viable NP in $\mathcal{C}_{10}^{(j)}$ can cause a signal [9], also Fig. 2. Secondly, and this holds of course in general

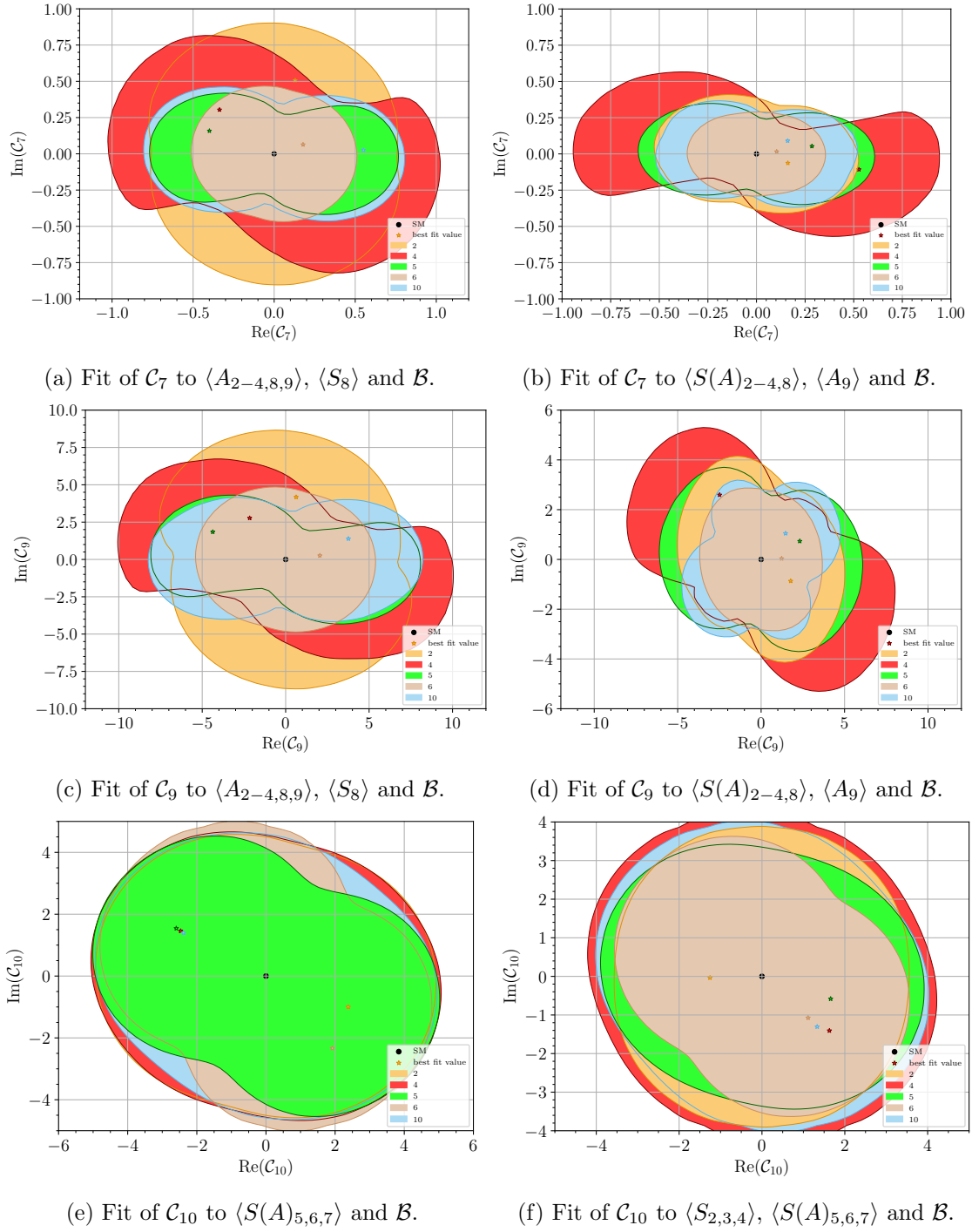


Figure 5: Fits of C_7 , C_9 , and C_{10} in fit scenarios 2,4,5,6 and 10, representing the groups with similar fit parameters, see main text.

for null tests, but is very critical for $D \rightarrow \pi^+ \pi^- \mu^+ \mu^-$ decays, the sensitivity to NP, i.e. the smallest value of a NP coefficient that causes a null test observation, is lower than the limit derived from non-observation of a NP signal. The difference between these two is given by

the SM uncertainties from strong phases, whose impact is pronounced in the null tests. For the case of 4-body decays and resonances in more than one channel, these are substantial, as discussed in Sec. 4.1.

While constraints from $D \rightarrow \pi^+\pi^-\mu^+\mu^-$ observables are weaker compared to those from other decays, the rich structure of the differential distribution of the 4-body decay complements other $c \rightarrow u\ell^+\ell^-$ observables. This aids to resolve flat directions in the global fit, see Sec. 6.2 for further details.

4.3 Beyond S- and P-wave

Because of the issues of the SM fit discussed in Sec. 4.1, we consider additional contributions beyond the resonance ansatz (3.33).

We begin analyzing the impact of D-wave resonances such as the $f_2(1270)$, which decays mostly to $\pi\pi$. Due to its high mass, it mostly contributes to low q^2 [9]. We find that $\langle S_{8,9} \rangle = 0$ even for D-waves assuming universality between different polarizations. The observables $\langle S_{2,3,4} \rangle$ receive D-wave contributions, specifically $\langle S_2 \rangle_D \sim (|\mathcal{F}_{\parallel D}|^2 + |\mathcal{F}_{\perp D}|^2 - 3|\mathcal{F}_{0D}|^2)$, $\langle S_3 \rangle_D \sim (|\mathcal{F}_{\parallel D}|^2 - |\mathcal{F}_{\perp D}|^2)$ and $\langle S_4 \rangle_D \sim \text{Re}(\mathcal{F}_{0D}\mathcal{F}_{\parallel D}^*)$, as well as a D - S -interference contribution only for $\langle S_4 \rangle_{D-S} \sim \text{Re}(\mathcal{F}_{0S}\mathcal{F}_{\parallel D}^*)$ [37]. However, we could not identify some parameter region for the D-wave that significantly affects $\langle S_4 \rangle$, as desirable, see Fig. 4, while leaving $\langle S_{2,3} \rangle$ unchanged, or not altering the differential branching fraction. Likewise, an improvement of the SM prediction of the differential branching ratio does not appear to be possible with the f_2 resonance as its mass is above the region $\sqrt{p^2} \in [0.8, 1.1]$ GeV in which the decay distributions are difficult to explain, see Fig. 3.

Bremsstrahlung contributions have been estimated in Ref. [42] through Low's theorem and although they appear in all angular observables except the null tests they are restricted to low q^2 and are too small to address the discrepancies in the differentials. Although $\langle S_9 \rangle$ receives contributions, they are negligible for high- q^2 and the tension with the experimental data similar to $\langle S_{2,4} \rangle$ remains.

Cascade contributions $D^0 \rightarrow \pi^\mp a_1^\pm (\rightarrow \pi^\pm \rho^0 (\rightarrow \mu^+ \mu^-))$ could play a significant role as their branching fractions are sizeable.⁶ However they are more difficult to model than the S- and P-wave resonances and beyond the scope of this work. Nevertheless an experimental double differential including correlations would be useful to decipher the resonances and to perform studies on these cascade contributions in the future.

5 Global $c \rightarrow u$ fits

We perform one-dimensional (1D) and two-dimensional (2D) fits for various combinations and subsets of NP Wilson coefficients $\mathcal{C}_7^{(\prime)}$, $\mathcal{C}_9^{(\prime)}$, and $\mathcal{C}_{10}^{(\prime)}$ using experimental information from $|\Delta c| = |\Delta u| = 1$ transitions, branching ratio data of $D \rightarrow \mu^+\mu^-$ [14], $D^+ \rightarrow \pi^+\mu^+\mu^-$ [24], $\Lambda_c \rightarrow p\mu^+\mu^-$ [13], and branching ratios [40] and angular observables [36] of $D \rightarrow \pi^+\pi^-\mu^+\mu^-$ decays. We use the same fit procedure as Ref. [41]. Resonances in $D \rightarrow \pi^+\pi^-\mu^+\mu^-$ decays are described with the best-fit values of scenario 4, see Sec. 4.1.

⁶We believe that the first mention of axial-vector resonance contributions is by Oscar Cata.

1D and 2D fit results are given in Secs 5.1 and 5.2, respectively. The main results of the fits are presented in Tabs. 3 and 4. Constraints on the NP Wilson coefficients are given at the charm mass scale μ_c .

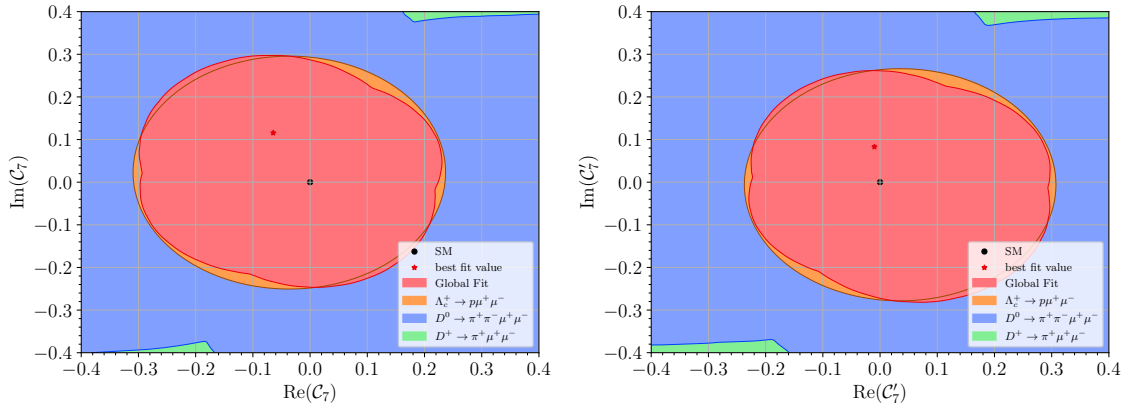


Figure 6: 2D fits to \mathcal{C}_7 (left panel) and \mathcal{C}'_7 (right panel), corresponding to scenarios H_{13} and H_{16} in Tab. 4. Shown are the 1σ allowed regions of the individual observables and the combined 1σ region (red). The red (black) star represents the best-fit (SM) value.

5.1 One-dimensional fits

The 1D fit results are reported in Tab. 3. The first column lists the names ($H_{1,\dots,12}$), followed by the second column with the Wilson coefficient that is fitted. The best-fit values, along with their 1σ and 2σ confidence intervals, are provided in the third, fourth and fifth columns, respectively. The last two columns give the goodness-of-fit indicators, including the best-fit χ^2 value and the p -value of the fit.

We recall that in a specific fit we only include observables which depend on the fit parameters, that is, the degrees of freedom in general vary between the different fits. The χ^2 value of the SM hypothesis is $\chi^2_{\text{SM}} = 17.0$ for fits to $\mathcal{C}_7^{(l)}$ or $\mathcal{C}_9^{(l)}$ and $\chi^2_{\text{SM}} = 22.3$ for fits to $\mathcal{C}_{10}^{(l)}$. In all cases, the minimal χ^2 values in the fit scenarios $\chi^2_{H_i, \text{min}}$ are close to the corresponding SM one, hence, the fits are good, supporting the SM and allowing one to put robust constraints on NP.

5.2 Two-dimensional fits

We explore scenarios consisting of pairs of coefficients from $\mathcal{C}_7^{(l)}$, $\mathcal{C}_9^{(l)}$, $\mathcal{C}_{10}^{(l)}$ in $H_{13,\dots,22}$. The results of the 2D fits are presented in Tab. 4. The χ^2 value of the SM hypothesis for fits involving $\mathcal{C}_7^{(l)}$ and $\mathcal{C}_{10}^{(l)}$, or $\mathcal{C}_9^{(l)}$ and $\mathcal{C}_{10}^{(l)}$ is $\chi^2_{\text{SM}} = 37.4$. As for the 1D case we obtain good fits, and consistency with the SM.

In Figs. 6 and 7 we show the allowed regions for 2D fits, for coefficients of dipole $\mathcal{C}_7^{(l)}$ and of semi-leptonic operators $\mathcal{C}_{9,10}^{(l)}$, respectively. Also shown in Fig. 7 are constraints on $\text{Re}(\mathcal{C}'_9 + \mathcal{C}'_{10})$ vs $\text{Re}(\mathcal{C}'_9 - \mathcal{C}'_{10})$, illustrating constraints for right-handed up-type quarks and left- and right-handed leptons. This corresponds to a simplified $SU(2)_L$ -invariant setting where renormalization group effects from the NP scale Λ_{NP} down to the electroweak

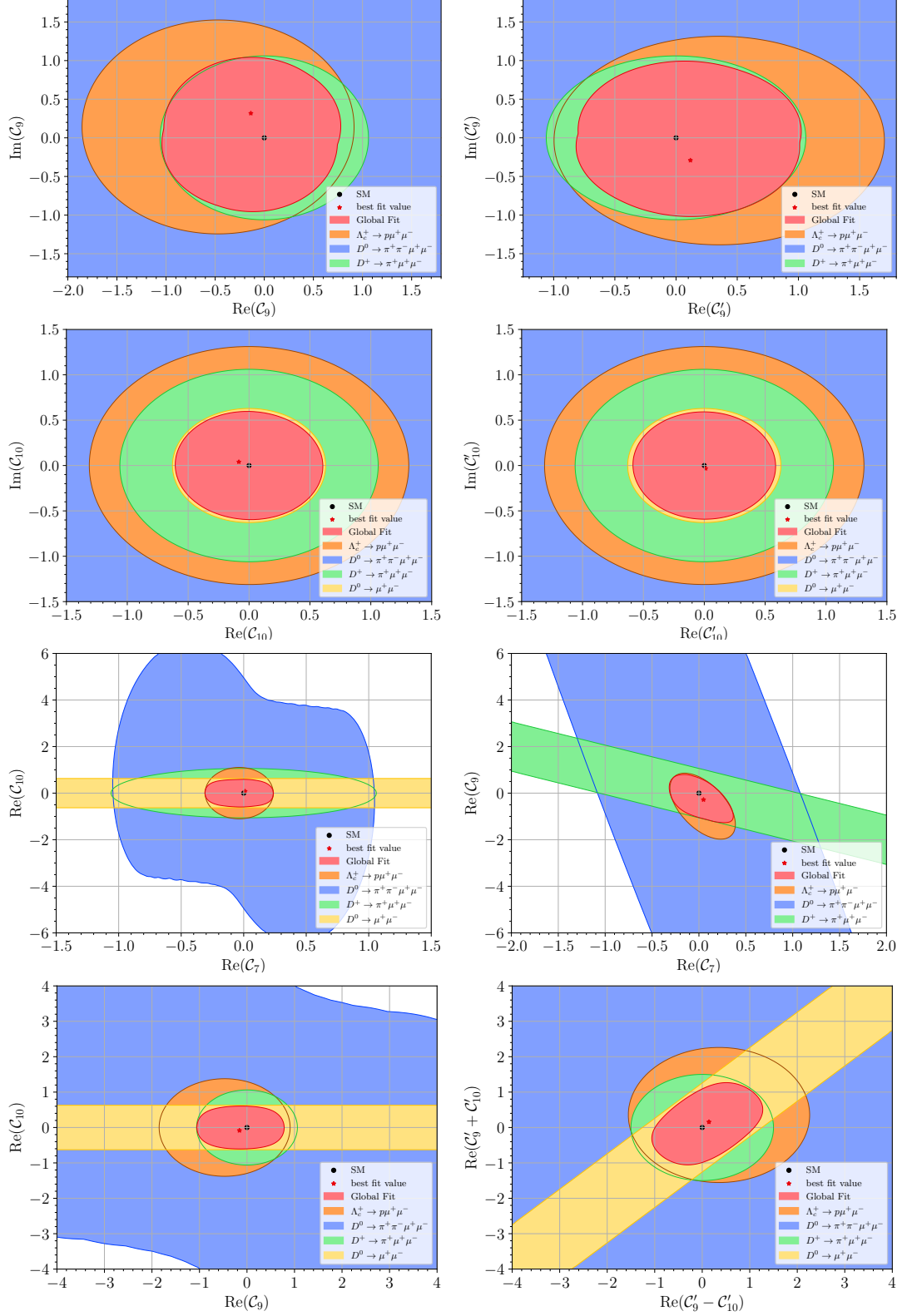


Figure 7: Contours of the 2D fits to semileptonic four-fermion operators, and mixed ones on $(\text{Re} C_7, \text{Re} C_{10})$, and $(\text{Re} C_7, \text{Re} C_9)$, see Tab. 4. Also shown in the bottom right plot is $\text{Re}(C'_9 + C'_{10})$ vs $\text{Re}(C'_9 - C'_{10})$; similar description as Fig. 6.

scenario	fit parameter	best fit	1σ	2σ	$\chi^2_{H_i, \min}$	p -value (%)
H_1	$\text{Re } \mathcal{C}_7$	0.01	[-0.26,+0.18]	[-0.35,+0.28]	17.0	91.1
H_2	$\text{Re } \mathcal{C}_9$	-0.21	[-0.85,+0.55]	[-1.2,+0.95]	16.9	91.2
H_3	$\text{Re } \mathcal{C}_{10}$	-0.09	[-0.50,+0.50]	[-0.71,+0.71]	22.3	76.8
H_4	$\text{Re } \mathcal{C}'_7$	0.05	[-0.18,+0.25]	[-0.28,+0.35]	16.9	91.2
H_5	$\text{Re } \mathcal{C}'_9$	0.15	[-0.61,+0.82]	[-1.0,+1.2]	16.9	91.1
H_6	$\text{Re } \mathcal{C}'_{10}$	0.00	[-0.45,+0.45]	[-0.69,+0.69]	22.3	76.7
H_7	$\text{Im } \mathcal{C}_7$	0.09	[-0.20,+0.24]	[-0.29,+0.33]	16.6	92.1
H_8	$\text{Im } \mathcal{C}_9$	0.32	[-0.76,+0.85]	[-1.1,+1.2]	16.8	91.5
H_9	$\text{Im } \mathcal{C}_{10}$	0.06	[-0.47,+0.47]	[-0.69,+0.70]	22.3	76.7
H_{10}	$\text{Im } \mathcal{C}'_7$	-0.09	[-0.22,+0.21]	[-0.31,+0.30]	16.6	92.0
H_{11}	$\text{Im } \mathcal{C}'_9$	-0.28	[-0.82,+0.80]	[-1.2,+1.1]	16.8	91.5
H_{12}	$\text{Im } \mathcal{C}'_{10}$	-0.03	[-0.46,+0.46]	[-0.69,+0.69]	22.3	76.7

Table 3: Fit results for Wilson coefficients in the 1D scenarios ($H_{1,\dots,12}$) at the scale μ_c . Best-fit values and 1σ (2σ) uncertainties are displayed in the third and fourth (fifth) columns. The indicators of the goodness-of-fit are provided in the last columns, the χ^2 function evaluated at the best-fit point and the p -value.

scale have not been included. The latter are, however, small, less than 5% for $\Lambda_{\text{NP}} = 10 \text{ TeV}$ [43]. High- p_T Drell-Yan tails also provide constraints on semileptonic 4-fermion $|\Delta c| = |\Delta u| = 1$ operators in this framework, however, they are insensitive to interference effects [44]. Assuming $SU(2)_L$, operators with left-handed charm quarks are subject to strong constraints from kaon decays [45].

As already anticipated in Sec. 4.2 the global fit is dominated by 2- und 3-body decays, and $D \rightarrow \pi^+ \pi^- \mu^+ \mu^-$ is not competitive. If dipole operators are present, the most important constraint is from the $\Lambda_c \rightarrow p \mu^+ \mu^-$ branching ratio. In fits with $\mathcal{C}_{10}^{(\prime)}$, the strongest constraint is from $D \rightarrow \mu^+ \mu^-$; for $\mathcal{C}_9, \mathcal{C}_{10}$ the $D^+ \rightarrow \pi^+ \mu^+ \mu^-$ data is the most constraining, followed by data on the baryonic decays.

6 Future prospects

We study future perspectives of the $|\Delta c| = |\Delta u| = 1$ global fit. We analyze the physics potential of $\Lambda_c \rightarrow p \ell^+ \ell^-$ decays in Sec. 6.1. In Sec. 6.2 we work out complementarities between 2-, 3- and 4-body $c \rightarrow u \mu^+ \mu^-$ decays.

scen.	fit parameters	best fit	1σ	2σ	$\chi^2_{H_i, \min}$	p -v. (%)
H_{13}	(Re C_7 , Im C_7)	(-0.06,+0.12)	([-0.24,+0.17],[-0.19,+0.25])	([-0.34,+0.27],[-0.29,+0.33])	16.5	90.0
H_{14}	(Re C_9 , Im C_9)	(-0.14,+0.32)	([-0.82,+0.55],[-0.76,+0.86])	([-1.2,+0.94],[-1.1,+1.2])	16.8	89.0
H_{15}	(Re C_{10} , Im C_{10})	(-0.09,+0.04)	([-0.48,+0.48],[-0.46,+0.46])	([-0.70,+0.70],[-0.69,+0.69])	22.3	72.3
H_{16}	(Re C'_7 , Im C'_7)	(-0.01,0.08)	([-0.17,+0.24],[-0.24,+0.22])	([-0.27,+0.34],[-0.32,+0.30])	16.6	89.4
H_{17}	(Re C'_9 , Im C'_9)	(+0.12,-0.29)	([-0.58,+0.80],[-0.83,+0.80])	([-0.99,+1.2],[-1.2,+1.1])	16.8	88.9
H_{18}	(Re C'_{10} , Im C'_{10})	(+0.01,-0.032)	([-0.45,+0.45],[-0.46,+0.46])	([-0.69,+0.68],[-0.69,+0.69])	22.3	72.1
H_{19}	(Re C_7 , Re C_9)	(+0.049,-0.28)	([-0.26,+0.29],[-1.0,+0.56])	([-0.36,+0.42],[-1.5,+0.98])	16.9	88.7
H_{20}	(Re C_7 , Re C_{10})	(+0.01,+0.08)	([-0.26,+0.18],[-0.48,+0.47])	([-0.35,+0.28],[-0.69,+0.69])	37.4	90.6
H_{21}	(Re C_9 , Re C_{10})	(-0.16,-0.09)	([-0.85,+0.55],[-0.48,+0.48])	([-1.2,+1.0],[-0.70,+0.70])	37.3	90.7
H_{22}	(Re $\{C'_9 - C'_{10}\}$, Re $\{C'_9 + C'_{10}\}$)	(0.14,0.15)	([-0.75,1.0],[-0.75,1.0])	([-1.3,1.5],[-1.3,1.5])	37.4	90.6

Table 4: 2D fit results with similar description as Tab. 3.

6.1 $\Lambda_c \rightarrow p \ell^+ \ell^-$ physics potential

To study the future sensitivity of $\Lambda_c \rightarrow p \ell^+ \ell^-$ we define CP-symmetries and CP-asymmetries of the binned forward-backward asymmetry (3.17), (3.18) as

$$\Delta \langle A_{\text{FB}} \rangle_{[q_{\min}^2, q_{\max}^2]} = \frac{1}{2} \left(\langle A_{\text{FB}} \rangle_{[q_{\min}^2, q_{\max}^2]} + \langle \bar{A}_{\text{FB}} \rangle_{[q_{\min}^2, q_{\max}^2]} \right), \quad (6.1)$$

$$\Sigma \langle A_{\text{FB}} \rangle_{[q_{\min}^2, q_{\max}^2]} = \frac{1}{2} \left(\langle A_{\text{FB}} \rangle_{[q_{\min}^2, q_{\max}^2]} - \langle \bar{A}_{\text{FB}} \rangle_{[q_{\min}^2, q_{\max}^2]} \right). \quad (6.2)$$

Since A_{FB} is CP-odd, $\Delta \langle A_{\text{FB}} \rangle$ is a CP-asymmetry and $\Sigma \langle A_{\text{FB}} \rangle$ the CP-average. Looking only at the C_{10} contribution and using $K_{1c} \propto \text{Re}(C_9^R C_{10}^*)$ [26], one obtains $\Delta \langle A_{\text{FB}} \rangle \propto \text{Im}(C_{10})$ and $\Sigma \langle A_{\text{FB}} \rangle \propto \text{Re}(C_{10})$.

The values of $\Delta \langle A_{\text{FB}} \rangle$ and $\Sigma \langle A_{\text{FB}} \rangle$ depend strongly on the strong phases δ_ρ , δ_ω and δ_ϕ . The isospin relation fixes the relative phase $\delta_\rho - \delta_\omega = \pi$ and a more precise measurement of the branching ratio constrains the relative phase $\delta_\phi - \delta_\rho$, see Fig. 1. The remaining overall phase of the resonances C_9^R which one could choose to be δ_ϕ , is actually a relative strong phase with respect to the NP contribution and affects A_{FB} . However, as it enters in the branching ratio only in subdominant interference terms it cannot be efficiently constrained with branching ratio data, and remains as one of the dominant uncertainties in A_{FB} .

In Tab. 5 we provide branching ratios and $\Sigma \langle A_{\text{FB}} \rangle$ for various bins and benchmark values of C_{10} , with varied strong phases. Besides the q^2 -bins considered in [13, 26], we introduce additional ones to increase the NP reach. Specifically, we separate the resonance contributions into a bin above ‘right’ and one below ‘left’ to avoid cancellations from sign changes close to the resonances $m_{\omega, \rho}^2 \sim 0.613 \text{ GeV}^2$ or $m_\phi^2 \sim 1.039 \text{ GeV}^2$. We further explore the bins “ ω/ρ left optimized” and “ ϕ right optimized”, which extend to the kinematic endpoints and have cuts around the resonances to increase the sensitivity of $\langle A_{\text{FB}} \rangle$. As a trade-off, the branching fraction decreases. As the impact of NP on the branching ratio is negligible, $\langle A_{\text{FB}} \rangle$ scales linearly with C_{10} . The sole exception is the $\sqrt{q^2} > 1.25 \text{ GeV}$ bin for largish NP coefficient $C_{10} = 0.30$ near maximum (3.9). However, even in this case $\mathcal{B} = [0.5, 2.2] \times 10^{-9}$, which is close to the SM value.

bin	q^2 / GeV^2 region	$\mathcal{B}_{\text{SM,bin}}$	$\langle A_{\text{FB}} \rangle_{\text{bin}}, \mathcal{C}_{10} = 0.30$	$\langle A_{\text{FB}} \rangle_{\text{bin}}, \mathcal{C}_{10} = 0.05$
ω/ρ left optimized	[0.045, 0.478]	$[0.15, 0.41] \times 10^{-7}$	[-0.06, 0.06]	[-0.010, 0.010]
ω/ρ left	[0.346, 0.613]	$[0.58, 1.07] \times 10^{-7}$	[-0.029, 0.029]	[-0.005, 0.005]
ω/ρ right	[0.613, 0.932]	$[0.41, 1.05] \times 10^{-7}$	[-0.05, 0.05]	[-0.009, 0.009]
ρ part 2 [13]	[0.677, 0.932]	$[0.15, 0.67] \times 10^{-7}$	[-0.10, 0.10]	[-0.017, 0.017]
ϕ [13]	[0.959, 1.122]	$[2.3, 3.7] \times 10^{-7}$	[-0.011, 0.011]	[-0.0018, 0.0018]
ϕ left	[0.959, 1.039]	$[1.0, 2.0] \times 10^{-7}$	[-0.018, 0.018]	[-0.0030, 0.0030]
ϕ right	[1.039, 1.122]	$[1.1, 2.0] \times 10^{-7}$	[-0.018, 0.018]	[-0.0031, 0.0031]
ϕ right optimized	[1.052, 1.818]	$[0.15, 0.70] \times 10^{-7}$	[-0.10, 0.10]	[-0.017, 0.017]
$\sqrt{q^2} > 1.25 \text{ GeV}$ [26]	[1.562, 1.818]	$[0.11, 1.84] \times 10^{-9}$	[-0.29, 0.29]	[-0.14, 0.14]

Table 5: \mathcal{B} and $\langle A_{\text{FB}} \rangle$ in $\Lambda_c \rightarrow p \mu^+ \mu^-$ decays for different q^2 bins and NP benchmarks. We explore bins to the left (below $q^2 = m_R^2$) and to the right (above $q^2 = m_R^2$) of a resonance to prevent large cancellations from A_{FB} changing sign, and further optimized ones to increase the NP signal (compare ϕ right optimized and ϕ right). NP effects in the branching ratio are negligible except for the $\sqrt{q^2} > 1.25 \text{ GeV}$ bin and $\mathcal{C}_{10} = 0.30$ for which it is within $[0.5, 2.2] \times 10^{-9}$.

As $\langle A_{\text{FB}} \rangle$ is normalized to the branching ratio, generically a bin with a small branching ratio has a large asymmetry, and vice versa. An extreme case is the $\sqrt{q^2} > 1.25 \text{ GeV}$ bin, with branching ratio of up to 2×10^{-9} , and an asymmetry $\langle A_{\text{FB}} \rangle \lesssim (1 - 3) \cdot \mathcal{C}_{10}$. On the other hand, the NP sensitivity depends also on the resonance dynamics. In the “ ϕ right optimized”-bin or the ‘ ρ part 2’-bin with larger branching ratios, reaching 10^{-7} , we find $\langle A_{\text{FB}} \rangle \lesssim 0.3 \cdot \mathcal{C}_{10}$. Other bins have similar branching ratios, but less efficient transfer of NP, for instance, the other ϕ bins have $\langle A_{\text{FB}} \rangle \lesssim 0.06 \cdot \mathcal{C}_{10}$ or less.

To study the impact of a future measurement of $\langle A_{\text{FB}} \rangle$, we assume that, in each of the bins used, the $\Lambda_c \rightarrow p \mu^+ \mu^-$ branching ratio is measured with a precision of $\Delta\mathcal{B}/\mathcal{B} = 7\%$ (2%). Using Gaussian-error propagation, we approximate the corresponding experimental sensitivity in $\langle A_{\text{FB}} \rangle$ as $\Delta\mathcal{B}/\mathcal{B} = 7\%$ (2%). This implies sensitivity to NP contributions in $\mathcal{C}_{10} \sim 0.2$ (0.06) from one of the best bins, i.e., the “ ϕ right optimized”-bin or the ‘ ρ part 2’, see Tab. 5. The sensitivity is set by the highest sensitivity of a single null test observable. This reach can be matched from $D \rightarrow \mu^+ \mu^-$ if the present limit (3.7) is improved by a factor 7 (75). We recall complementarity of the decay modes in the presence of both \mathcal{C}_{10} and \mathcal{C}'_{10} . We study this also further in Sec. 6.2. Also note that $\mathcal{B}(D \rightarrow \mu^+ \mu^-)$ is quadratic in the NP coefficient, while the null test $\langle A_{\text{FB}} \rangle$ is linear, hence favorable for smaller NP contributions.

Working out upper limits is more involved due to correlations between bins and observables and accidental suppressions by phase tunings. Recall that a single observable, $\Sigma\langle A_{\text{FB}} \rangle$ or $\Delta\langle A_{\text{FB}} \rangle$ in a single bin, can give a null result even in the presence of large NP

with tuning between the overall resonance phase and NP, see also footnote 4. On the other hand, measurements of both $\Sigma\langle A_{\text{FB}}\rangle$ and $\Delta\langle A_{\text{FB}}\rangle$ in more than a single bin fixes this and prevents flat directions. Improvements of NP constraints are therefore not only driven by the most precise measurement but rather by multiple measurements and their correlations with the strong phases. We emphasize that this assumes negligible kinematic dependence of the strong phases, as in the ansatz (3.33).

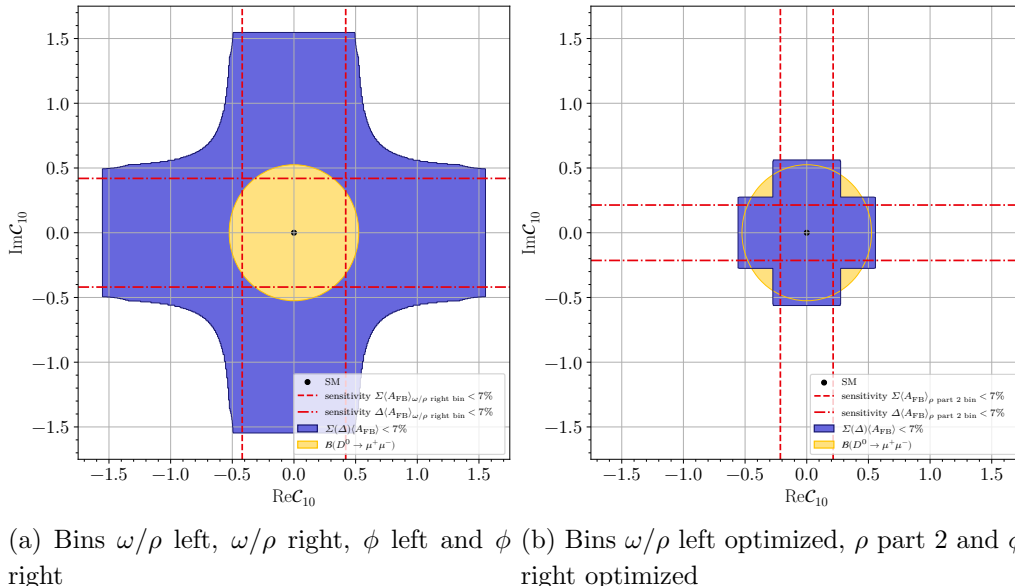


Figure 8: Allowed region of (blue area) and sensitivity to (red lines) \mathcal{C}_{10} with future measurements of $\Sigma\langle A_{\text{FB}}\rangle$ and $\Delta\langle A_{\text{FB}}\rangle$ at the level of 7% in each bin used, as specified in the captions, and with bins defined in Tab. 5. In the right panel (b) optimized bins are used which improve the NP reach compared to bins in panel (a). The yellow circle denotes the allowed region by current data on $\mathcal{B}(D \rightarrow \mu^+\mu^-)$.

In Fig. 8 we show the allowed region of \mathcal{C}_{10} from current data on $D^0 \rightarrow \mu^+\mu^-$ (3.8) (yellow), and compare it to the one from a hypothetical limit on $\Sigma\langle A_{\text{FB}}\rangle$ and $\Delta\langle A_{\text{FB}}\rangle$ at the level of 7% (blue) using the bins ω/ρ left, ω/ρ right, ϕ left and ϕ right (left panel (a)) or ω/ρ left optimized, ρ part 2, and ϕ right optimized (right panel (b)) from Tab. 5. The symmetry of the blue cross results from invariance of $\Sigma\langle A_{\text{FB}}\rangle$ and $\Delta\langle A_{\text{FB}}\rangle$ under a simultaneous sign change of \mathcal{C}_{10} and $\delta_{\rho,\omega,\phi} \rightarrow \delta_{\rho,\omega,\phi} + \pi$ [26]. Comparison of Fig. 8 (a) to (b) confirms that the optimized bins used in (b) have better NP reach, with a factor three improvement on the upper limits. The sensitivity to NP from the hypothetical measurements of $\Sigma\langle A_{\text{FB}}\rangle$ or $\Delta\langle A_{\text{FB}}\rangle$ is shown by red vertical and horizontal lines. As already argued in Sec. 4.2 for null tests in $D \rightarrow \pi^+\pi^-\mu^+\mu^-$, the upper limits on the Wilson coefficients are larger than the sensitivity.

6.2 Complementarity

We analyze the complementarity between the decay modes for the NP coefficients $\text{Re} \{ \mathcal{C}_{10} \pm \mathcal{C}'_{10} \}$ of the GIM-protected operators $\mathcal{O}_{10}, \mathcal{O}'_{10}$. They enter the observables as follows

$$\begin{aligned}
\mathcal{B}(D \rightarrow \mu^+ \mu^-) &\propto |\mathcal{C}_{10} - \mathcal{C}'_{10}|^2, \\
\mathcal{B}(D \rightarrow \pi \mu^+ \mu^-)_{\text{NP}} &\propto |\mathcal{C}_{10} + \mathcal{C}'_{10}|^2, \\
\mathcal{B}(\Lambda_c \rightarrow p \mu^+ \mu^-)_{\text{NP}} &\propto |\mathcal{C}_{10} \pm \mathcal{C}'_{10}|^2, \\
\Sigma \langle A_{\text{FB}}(\Lambda_c \rightarrow p \mu^+ \mu^-) \rangle &\propto \text{Re } \mathcal{C}_{10}, \\
\Delta \langle A_{\text{FB}}(\Lambda_c \rightarrow p \mu^+ \mu^-) \rangle &\propto \text{Im } \mathcal{C}_{10}, \\
I_7(D \rightarrow \pi \pi \mu^+ \mu^-) &\propto \text{Re}, \text{Im} \{ \mathcal{C}_{10} - \mathcal{C}'_{10} \}, \\
I_{5,6}(D \rightarrow \pi \pi \mu^+ \mu^-) &\propto \text{Re}, \text{Im} \{ \mathcal{C}_{10} \pm \mathcal{C}'_{10} \}.
\end{aligned} \tag{6.3}$$

For the angular observables we only give those terms that interfere with \mathcal{C}_9^R to indicate resonance enhancement and omit here possible subleading NP effects in the denominators, that is, the branching ratios. We include them however in the numerics to prohibit artifacts in the fit. Note that then angular observables (6.3) are linear in NP, whereas branching ratios are quadratic, making the ratio-type observables more sensitive to smaller NP coefficients. If both \pm signs are present their relative strength depends on the hierarchy and interplay of transversity amplitudes, which depend on form factors and the q^2 -region.

Current constraints on the branching ratios of $D \rightarrow \mu^+ \mu^-$ (yellow), $D^+ \rightarrow \pi^+ \mu^+ \mu^-$ (green) and $\Lambda_c \rightarrow p \mu^+ \mu^-$ (orange) are shown in Fig. 9. Also shown is the impact of future null test measurements $\Sigma \langle A_{\text{FB}} \rangle$ at 7% level (dark blue), as in Fig. 8, and the $D \rightarrow \pi^+ \pi^- \mu^+ \mu^-$ -observable $\langle S_5 \rangle$ at 0.7% for illustration in the $\sqrt{q^2}$ -bin [0.565-0.780] GeV (light blue) for fixed strong phases $\delta_{P,\phi} = \delta_{S,\phi} = 2/5\pi$ and $\delta_i = \delta_{i,\text{best-fit}} + \delta_{P,\phi}$ for all others, assuming they are known from other observables of the 4-body decay. Therefore, SM uncertainties are significantly reduced and the upper limits are close to the sensitivity to NP. Note, other q^2 bins would exhibit different slopes in the $\text{Re} \{ \mathcal{C}_{10} \pm \mathcal{C}'_{10} \}$ -plane. We illustrate the potential of $D \rightarrow \pi^+ \pi^- \mu^+ \mu^-$ with the angular coefficient I_5 , because I_7 is sensitive to the difference of \mathcal{C}_{10} and \mathcal{C}'_{10} , just like the $D \rightarrow \mu^+ \mu^-$ branching ratio, and I_6 probes also both linear combinations, although with $I_6 \sim H_{\parallel} H_{\perp}^*$ instead of $I_5 \sim H_0 H_{\perp}^*$, see (3.30), implying different form factors. As apparent from Fig. 9, each observable shown gives different type of constraints, demonstrating synergies between different decays.

In a $SU(2)_L$ -invariant setting, strong constraints from kaon decays on $\mathcal{C}_9 - \mathcal{C}_{10}$ from dineutrino decays and $\mathcal{C}_9 + \mathcal{C}_{10}$ for decays to dimuons exist [45]. Sizable NP in charm is then limited to the right-handed quark sector, here in \mathcal{C}'_{10} . In this case $I_{5,6,7}$ in $D \rightarrow \pi^+ \pi^- \mu^+ \mu^-$ are still resonance-enhanced, whereas A_{FB} in $\Lambda_c \rightarrow p \mu^+ \mu^-$ decays is not.

7 Conclusions

We perform the first global analysis of rare charm decays using multiple decays and observables to exploit complementarities to strengthen the bounds on $|\Delta c| = |\Delta u| = 1$ NP coefficients. The outcome of the 1D and 2D fits are given in Tab. 3 and Tab. 4, respectively.

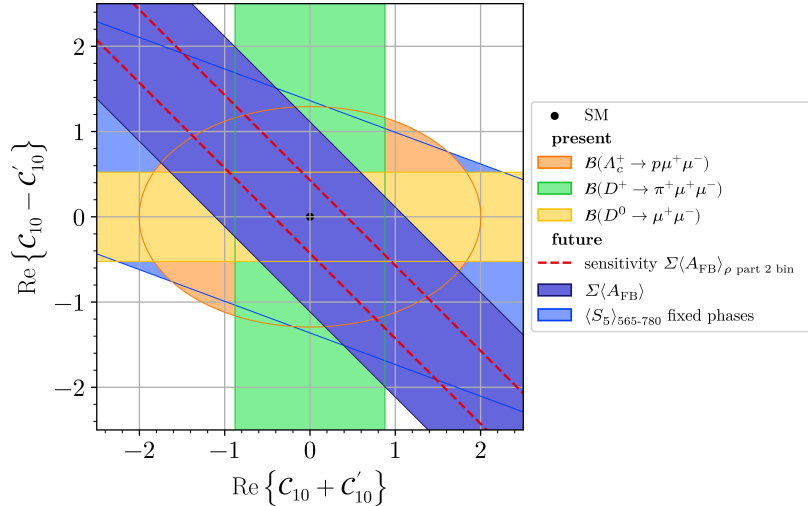


Figure 9: Complementarity of constraints in $\text{Re}\{C_{10} \pm C'_{10}\}$ from current branching ratio data on $D \rightarrow \mu^+\mu^-$ (yellow), $D^+ \rightarrow \pi^+\mu^+\mu^-$ (green) and $\Lambda_c \rightarrow p\mu^+\mu^-$ (orange), together with hypothetical future measurements of $\Sigma\langle A_{\text{FB}}\rangle$ at 7% level (dark blue) and $\langle S_5 \rangle$ at 0.7% (light blue), see text.

They are based on branching ratio data of $D \rightarrow \mu^+\mu^-$, $D \rightarrow \pi\mu^+\mu^-$, $D \rightarrow \pi^+\pi^-\mu^+\mu^-$ and $\Lambda_c \rightarrow p\mu^+\mu^-$ decays, and for the first time, angular observables, including the null test coefficients $I_{5,6,7}$ of $D \rightarrow \pi^+\pi^-\mu^+\mu^-$ decays. Let us summarize status and findings:

1. Null test observables are induced by NP, and amplified by interference with SM resonance amplitudes, see Fig. 2. Hence, the null tests exhibit resonance structure, and binning is key, as demonstrated in Fig. 8 for a future measurement of the forward-backward asymmetry in $\Lambda_c \rightarrow p\mu^+\mu^-$ decays. Choosing optimized q^2 -bins improves the limits on NP here by a factor of three.
2. While a null test can cleanly signal NP, an interpretation in terms of Wilson coefficients relies on the understanding of decay amplitudes. Requisite hadronic parameters of semileptonic $D \rightarrow \pi\mu^+\mu^-$, $D \rightarrow \pi^+\pi^-\mu^+\mu^-$ and $\Lambda_c \rightarrow p\mu^+\mu^-$ decays, which cannot be obtained with sufficient precision from other means, are extracted from observables which are largely insensitive to NP. These are generically differential branching ratios, with their characteristic resonance peaks as in Fig. 1.
3. We perform fits for $D \rightarrow \pi^+\pi^-\mu^+\mu^-$ decays in ten model scenarios to advance the theoretical description. We find, in agreement with [39], but in more general settings, that the measured differential decay spectra of $D \rightarrow \pi^+\pi^-\mu^+\mu^-$ in the dimuon and dipion mass [36] are difficult to match theoretically using scalar and vector resonances alone, see Fig. 3. An interesting outcome is that the fit with the best χ^2/dof , scenario 10, favors an effective contribution to the matrix element of \mathcal{O}_9 of about $r_9 \sim 2$, with an order one phase. Further study is desirable but beyond the scope of this work. The constraining-NP power of the 4-body decays, despite its many GIM-protected null

tests, is limited due to the complicated hadronic structure involving a large number of parameters, inducing significant hadronic uncertainties. In this way, $D \rightarrow \pi^+\pi^-\mu^+\mu^-$ is also a laboratory for hadronic dynamics, and probes different QCD frameworks, similar to the more simple radiative $D \rightarrow \pi\pi\gamma$ decays [23]. Improved data on the double differential decay rate $d^2\Gamma/dp^2dq^2$, including correlations provided by the experiment, would help here, as well as further modelling efforts.

4. Current constraints on NP are hence dominated by 2-body $D \rightarrow \mu^+\mu^-$ (if applicable, i.e. probing $\mathcal{C}_{10}-\mathcal{C}'_{10}$), and the 3-body decays, see Figs. 6 and 7, which displays synergies and added value between decay modes.
5. The decay $\Lambda_c \rightarrow p\mu^+\mu^-$ is the rising star with the simplicity of a 3-body decays and fewer hadronic parameters than multi-body decays however richer angular structure than $D \rightarrow \pi\mu^+\mu^-$. In particular, the baryonic decay features null test distributions, and has high sensitivity to radiative dipole operators at low q^2 via $\Lambda_c \rightarrow p\gamma^*$ [26].
6. Combination of various decay modes and observables allows to exploit complementarity, see Fig. 9. Due to its unique sensitivity to NP couplings in the angular distributions, $D \rightarrow \pi^+\pi^-\mu^+\mu^-$ decays have potential to become very important for searches in the high luminosity era. We hope to come back to a future version of the global fit with improved data, also on dielectron modes. Rare charm decays are suitable for study at LHCb [1], Belle II [2], and future colliders [4, 5], as well as high- p_T experiments such as CMS [14].

Acknowledgments

We thank Rigo Bause, Stefan de Boer, Marcel Golz, Tom Magorsch, Dominik Mitzel, Lara Nollen, Luiz Vale Silva and Eleftheria Solomonidi for useful discussions. The work of HG is supported by the European Union – NextGeneration EU and by the University of Padua under the 2021 STARS Grants@Unipd programme (Acronym and title of the project: CPV-Axion – Discovering the CP-violating axion) as well as by the European Union – Next Generation EU and by the Italian Ministry of University and Research (MUR) via the PRIN 2022 project n. 2022K4B58X – AxionOrigins. GH would like to thank the CERN Theory Department for kind hospitality and support during the finalization of this work.

A Form factors

Here we present the non-resonant and resonant form factors entering in Eqs. (B.1)-(B.9), Sections A.1 and A.2, respectively. In general the transversity form factors $\mathcal{F}_{0,\parallel,\perp}$ can be expanded in terms of the associated Legendre polynomials $P_\ell^m(\cos\theta_{P_1})$ and coefficients $F_{(0,\parallel,\perp),\ell}(q^2, p^2)$:

$$\begin{aligned}\mathcal{F}_0 &= \sum_{\ell=0} F_{0,\ell}(q^2, p^2) P_\ell^{m=0}(\cos\theta_{P_1}), \\ \mathcal{F}_\parallel &= \sum_{\ell=1} F_{\parallel,\ell}(q^2, p^2) \frac{P_\ell^{m=1}(\cos\theta_{P_1})}{\sin\theta_{P_1}}, \\ \mathcal{F}_\perp &= \sum_{\ell=1} F_{\perp,\ell}(q^2, p^2) \frac{P_\ell^{m=1}(\cos\theta_{P_1})}{\sin\theta_{P_1}},\end{aligned}\tag{A.1}$$

where the coefficients $F_{(0,\parallel,\perp),\ell}(q^2, p^2)$ can be calculated via the completeness relation

$$\begin{aligned}F_{0,\ell}(q^2, p^2) &= \frac{2\ell+1}{2} \int_{-1}^1 \mathcal{F}_0(q^2, p^2, \cos\theta_{P_1}) P_\ell^0(\cos\theta_{P_1}) d\cos\theta_{P_1}, \\ F_{(\parallel,\perp),\ell}(q^2, p^2) &= \frac{2\ell+1}{2} \frac{(\ell-1)!}{(\ell+1)!} \int_{-1}^1 \mathcal{F}_{\parallel,\perp}(q^2, p^2, \cos\theta_{P_1}) P_\ell^1(\cos\theta_{P_1}) \sin\theta_{P_1} d\cos\theta_{P_1}.\end{aligned}\tag{A.2}$$

A.1 Non-resonant form factors

The non-resonant transversity form factors are given by⁷

$$\begin{aligned}\mathcal{F}_0 &= \frac{\mathcal{N}_{\text{nr}}}{2} \left[\sqrt{\lambda_D} w_+ + \frac{1}{p^2} \left((m_{P_1}^2 - m_{P_2}^2) \sqrt{\lambda_D} - (m_D^2 - q^2 - p^2) \sqrt{\lambda_h} \cos\theta_{P_1} \right) w_- \right], \\ \mathcal{F}_\perp &= \frac{\mathcal{N}_{\text{nr}}}{2} \sqrt{\lambda_D \lambda_h} \frac{q^2}{p^2} h, \quad \mathcal{F}_\parallel = \mathcal{N}_{\text{nr}} \sqrt{\lambda_h} \frac{q^2}{p^2} w_-, \\ \mathcal{N}_{\text{nr}} &= \frac{G_F \alpha_e}{2^7 \pi^4 m_D} \sqrt{\pi} \frac{\sqrt{\lambda_D \lambda_h}}{m_D p^2},\end{aligned}\tag{A.3}$$

with $\lambda_D \equiv \lambda(m_D^2, q^2, p^2)$ and $\lambda_h \equiv \lambda(p^2, m_{P_1}^2, m_{P_2}^2)$ where $\lambda(a, b, c) \equiv a^2 + b^2 + c^2 - 2(ab + ac + bc)$ is the Källén function. For the form factors w_\pm and h we refer to [9].

A.2 Resonant form factors

In the following subsections, we present the P- and S-wave components $F_{(0,\parallel,\perp),P(S)}(q^2, p^2)$ of the resonant transversity form factors $\mathcal{F}_{0,P(S)}^{\text{res}}$, related via Eq. (A.1).

⁷To speed up the numerical integration, we expand the non-resonant transversity form factors $\mathcal{F}_{0,\parallel,\perp}$ in terms of $P_\ell^m(\cos\theta_{P_1})$ and $F_{(0,\parallel,\perp),\ell}(q^2, p^2)$ using Eqs. (A.1). This allows for analytical integration over $\cos\theta_{P_1}$. The coefficients $F_{(0,\parallel,\perp),\ell}(q^2, p^2)$ are computed using the completeness relation (A.2). Depending on the integration range of the observable, we expand to different orders in ℓ . This approximation is particularly effective for integrals of the form $\int_{-1}^{+1} f(\cos\theta_{P_1}) d\cos\theta_{P_1}$, where we consider $\ell \leq 3$. For $\left[\int_0^{+1} - \int_{-1}^0 \right] f(\cos\theta_{P_1}) d\cos\theta_{P_1}$, we require higher orders with $\ell \leq 6$.

A.2.1 P-wave

For the P-wave, we use the transversity form factors from Refs. [9, 39]:

$$\begin{aligned}
F_{0,P}^{\text{res}} &= -3\sqrt{\frac{3-\beta_\ell^2}{2}}N_V(p^2, q^2)\frac{(m_D^2-p^2-q^2)(m_D+m_{\rho^0})^2A_1(q^2)-\lambda_D A_2(q^2)}{2(m_D+m_{\rho^0})\sqrt{p^2q^2}P_{\rho^0/\omega}(p^2)}, \\
F_{\parallel,P}^{\text{res}} &= -\frac{3}{\sqrt{2}}N_V(p^2, q^2)\sqrt{\frac{3-\beta_\ell^2}{2}}\sqrt{2}(m_D+m_{\rho^0})\frac{A_1(q^2)}{P_{\rho^0/\omega}(p^2)}, \\
F_{\perp,P}^{\text{res}} &= \frac{3}{\sqrt{2}}N_V(p^2, q^2)\beta_\ell\frac{\sqrt{2\lambda_D}}{m_D+m_{\rho^0}}\frac{V(q^2)}{P_{\rho^0/\omega}(p^2)},
\end{aligned} \tag{A.4}$$

with

$$N_V = G_F\alpha_e\sqrt{\frac{\beta_\ell q^2\sqrt{\lambda_h\lambda_D}}{3(4\pi)^5 m_D^3 p^2}}, \quad \beta_\ell = \sqrt{1 - \frac{4m_\ell^2}{q^2}}. \tag{A.5}$$

Compared to the procedure employed in Ref. [9], the masses m_V^2 are replaced by p^2 , which is suitable for off-resonance effects following Ref. [39]. We take the $D \rightarrow \rho$ form factors $A_{1,2}, V$ from Ref. [46] and neglect differences to the $D \rightarrow \omega$ form factors.

For the p^2 line shape $P_{\rho^0/\omega}(p^2)$ we use the Gounaris-Sakurai line shape employed by Refs. [39, 47]:

$$\frac{1}{P_{\rho^0/\omega}(p^2)} = \frac{1}{\sqrt{\pi}}\frac{p^*(p^2)}{p_0^*}\frac{B(p^*)}{B(p_0^*)}\frac{1}{P_{\rho^0}(p^2)}\left(1 + a_{p^2,\omega}e^{i\delta_{p^2,\omega}}\text{RBW}_\omega(p^2)\right), \tag{A.6}$$

with $p^*(p^2) = \sqrt{\lambda(p^2, m_\pi^2, m_\pi^2)}/(2\sqrt{p^2})$, and $p_0^* = p^*(m_{\rho^0}^2)$. For the definitions of the functions in Eq. (A.6) see Ref. [39].

A.2.2 S-wave

For the S-wave expressions, we use Refs. [39, 48]

$$F_{0,S}^{\text{res}} = -N\frac{\sqrt{\beta_\ell(3-\beta_\ell^2)}\lambda_h^{1/4}\lambda_D^{3/4}}{2\sqrt{2}\sqrt{p^2}}\frac{\tilde{f}_+(q^2)}{P_\sigma(p^2)}, \quad N = \frac{\alpha_e G_F}{128\pi^{7/2}m_D^{3/2}}, \quad \tilde{f}_+(q^2) = \frac{1}{1 - \frac{q^2}{m_A^2}} \tag{A.7}$$

with $m_A = 2.42$ GeV. We use the same line shape $P_\sigma(p^2) = 1/\mathcal{A}_S(p^2)$ for the σ -resonance as in Ref. [39].

B $D \rightarrow P_1 P_2 \ell^+ \ell^-$ angular observables

We expand the angular observables of $D \rightarrow P_1 P_2 \ell^+ \ell^-$ in terms of the resonant S-, P-wave and non-resonant transversity form factors. Using Eq. (3.31) for the transversity

amplitudes the angular coefficients given by Eq. (3.30) become⁸

$$\begin{aligned}
I_1 = & +\frac{1}{8} \left| \mathcal{C}_9^{\mathcal{R},S} \right|^2 \left| \mathcal{F}_{0,S}^{\text{res}} \right|^2 + \left| \mathcal{C}_9^{\mathcal{R},P} \right|^2 \left(\frac{1}{8} \left| \mathcal{F}_{0,P}^{\text{res}} \right|^2 + \frac{3}{16} \left(\left| \mathcal{F}_{\parallel,P}^{\text{res}} \right|^2 + \left| \mathcal{F}_{\perp,P}^{\text{res}} \right|^2 \right) \sin^2 \theta_{P_1} \right) \\
& + \frac{1}{4} \text{Re} \left\{ \mathcal{C}_9^{\mathcal{R},P} \left(\mathcal{C}_9^{\mathcal{R},S} \right)^* \right\} \text{Re} \left[\mathcal{F}_{0,S}^{\text{res}} \mathcal{F}_{0,P}^{\text{res},*} \right] + \frac{1}{4} \text{Im} \left\{ \mathcal{C}_9^{\mathcal{R},P} \left(\mathcal{C}_9^{\mathcal{R},S} \right)^* \right\} \text{Im} \left[\mathcal{F}_{0,S}^{\text{res}} \mathcal{F}_{0,P}^{\text{res},*} \right] \\
& + \frac{3}{16} \rho_1^+ \left| \mathcal{F}_{\perp} \right|^2 \sin^2 \theta_{P_1} + \rho_1^- \left(\frac{1}{8} \left| \mathcal{F}_0 \right|^2 + \frac{3}{16} \left| \mathcal{F}_{\parallel} \right|^2 \sin^2 \theta_{P_1} \right) \\
& - \frac{1}{4} \text{Im} \rho_{3,S}^- \text{Im} \left[\mathcal{F}_{0,S}^{\text{res}} \mathcal{F}_0^* \right] + \frac{1}{4} \text{Re} \rho_{3,S}^- \text{Re} \left[\mathcal{F}_{0,S}^{\text{res}} \mathcal{F}_0^* \right] \\
& + \frac{3}{8} \left(\text{Re} \rho_{3,P}^+ \text{Re} \left[\mathcal{F}_{\perp,P}^{\text{res}} \mathcal{F}_{\perp}^* \right] - \text{Im} \rho_{3,P}^+ \text{Im} \left[\mathcal{F}_{\perp,P}^{\text{res}} \mathcal{F}_{\perp}^* \right] \right) \sin^2 \theta_{P_1} \\
& + \text{Im} \rho_{3,P}^- \left(-\frac{1}{4} \text{Im} \left[\mathcal{F}_{0,P}^{\text{res}} \mathcal{F}_0^* \right] - \frac{3}{8} \text{Im} \left[\mathcal{F}_{\parallel,P}^{\text{res}} \mathcal{F}_{\parallel}^* \right] \sin^2 \theta_{P_1} \right) \\
& + \text{Re} \rho_{3,P}^- \left(\frac{1}{4} \text{Re} \left[\mathcal{F}_{0,P}^{\text{res}} \mathcal{F}_0^* \right] + \frac{3}{8} \text{Re} \left[\mathcal{F}_{\parallel,P}^{\text{res}} \mathcal{F}_{\parallel}^* \right] \sin^2 \theta_{P_1} \right), \tag{B.1}
\end{aligned}$$

$$\begin{aligned}
I_2 = & -\frac{1}{8} \left| \mathcal{C}_9^{\mathcal{R},S} \right|^2 \left| \mathcal{F}_{0,S}^{\text{res}} \right|^2 + \left| \mathcal{C}_9^{\mathcal{R},P} \right|^2 \left(-\frac{1}{8} \left| \mathcal{F}_{0,P}^{\text{res}} \right|^2 + \frac{1}{16} \left(\left| \mathcal{F}_{\parallel,P}^{\text{res}} \right|^2 + \left| \mathcal{F}_{\perp,P}^{\text{res}} \right|^2 \right) \sin^2 \theta_{P_1} \right) \\
& - \frac{1}{4} \text{Re} \left\{ \mathcal{C}_9^{\mathcal{R},P} \left(\mathcal{C}_9^{\mathcal{R},S} \right)^* \right\} \text{Re} \left[\mathcal{F}_{0,S}^{\text{res}} \mathcal{F}_{0,P}^{\text{res},*} \right] - \frac{1}{4} \text{Im} \left\{ \mathcal{C}_9^{\mathcal{R},P} \left(\mathcal{C}_9^{\mathcal{R},S} \right)^* \right\} \text{Im} \left[\mathcal{F}_{0,S}^{\text{res}} \mathcal{F}_{0,P}^{\text{res},*} \right] \\
& + \frac{1}{16} \rho_1^+ \left| \mathcal{F}_{\perp} \right|^2 \sin^2 \theta_{P_1} + \rho_1^- \left(-\frac{1}{8} \left| \mathcal{F}_0 \right|^2 + \frac{1}{16} \left| \mathcal{F}_{\parallel} \right|^2 \sin^2 \theta_{P_1} \right) \\
& - \frac{1}{4} \text{Re} \rho_{3,S}^- \text{Re} \left[\mathcal{F}_{0,S}^{\text{res}} \mathcal{F}_0^* \right] + \frac{1}{4} \text{Im} \rho_{3,S}^- \text{Im} \left[\mathcal{F}_{0,S}^{\text{res}} \mathcal{F}_0^* \right] \\
& + \frac{1}{8} \left(\text{Re} \rho_{3,P}^+ \text{Re} \left[\mathcal{F}_{\perp,P}^{\text{res}} \mathcal{F}_{\perp}^* \right] - \text{Im} \rho_{3,P}^+ \text{Im} \left[\mathcal{F}_{\perp,P}^{\text{res}} \mathcal{F}_{\perp}^* \right] \right) \sin^2 \theta_{P_1} \\
& + \text{Im} \rho_{3,P}^- \left(\frac{1}{4} \text{Im} \left[\mathcal{F}_{0,P}^{\text{res}} \mathcal{F}_0^* \right] - \frac{1}{8} \text{Im} \left[\mathcal{F}_{\parallel,P}^{\text{res}} \mathcal{F}_{\parallel}^* \right] \sin^2 \theta_{P_1} \right) \\
& + \text{Re} \rho_{3,P}^- \left(-\frac{1}{4} \text{Re} \left[\mathcal{F}_{0,P}^{\text{res}} \mathcal{F}_0^* \right] + \frac{1}{8} \text{Re} \left[\mathcal{F}_{\parallel,P}^{\text{res}} \mathcal{F}_{\parallel}^* \right] \sin^2 \theta_{P_1} \right), \tag{B.2}
\end{aligned}$$

$$\begin{aligned}
I_3 = & \left[+\frac{1}{8} \rho_1^+ \left| \mathcal{F}_{\perp} \right|^2 - \frac{1}{8} \rho_1^- \left| \mathcal{F}_{\parallel} \right|^2 - \frac{1}{8} \left| \mathcal{C}_9^{\mathcal{R},P} \right|^2 \left(\left| \mathcal{F}_{\parallel,P}^{\text{res}} \right|^2 - \left| \mathcal{F}_{\perp,P}^{\text{res}} \right|^2 \right) \right. \\
& + \frac{1}{4} \text{Im} \rho_{3,P}^- \text{Im} \left[\mathcal{F}_{\parallel,P}^{\text{res}} \mathcal{F}_{\parallel}^* \right] - \frac{1}{4} \text{Im} \rho_{3,P}^+ \text{Im} \left[\mathcal{F}_{\perp,P}^{\text{res}} \mathcal{F}_{\perp}^* \right] \\
& \left. - \frac{1}{4} \text{Re} \rho_{3,P}^- \text{Re} \left[\mathcal{F}_{\parallel,P}^{\text{res}} \mathcal{F}_{\parallel}^* \right] + \frac{1}{4} \text{Re} \rho_{3,P}^+ \text{Re} \left[\mathcal{F}_{\perp,P}^{\text{res}} \mathcal{F}_{\perp}^* \right] \right] \sin^2 \theta_{P_1}, \tag{B.3}
\end{aligned}$$

⁸For simplicity, we do not give the explicit contribution from dipole operators $\mathcal{C}_7^{(\prime)}$, but they can be included via the following shift $\mathcal{C}_{\pm}^{L,R}(q^2) \rightarrow \mathcal{C}_{\pm}^{L,R}(q^2) + \kappa \frac{2m_e m_D}{q^2} (\mathcal{C}_7 \pm \mathcal{C}'_7)$.

$$\begin{aligned}
I_4 = & \left[-\frac{1}{4} \left| \mathcal{C}_9^{\mathcal{R},P} \right|^2 \operatorname{Re}[\mathcal{F}_{0,P}^{\text{res}} \mathcal{F}_{\parallel,P}^{\text{res},*}] - \frac{1}{4} \rho_1^- \operatorname{Re}[\mathcal{F}_0 \mathcal{F}_{\parallel}^*] \right. \\
& + \frac{1}{4} \operatorname{Im} \left\{ \mathcal{C}_9^{\mathcal{R},P} \left(\mathcal{C}_9^{\mathcal{R},S} \right)^* \right\} \operatorname{Im}[\mathcal{F}_{\parallel,P}^{\text{res}} \mathcal{F}_{0,S}^{\text{res},*}] - \frac{1}{4} \operatorname{Re} \left\{ \mathcal{C}_9^{\mathcal{R},P} \left(\mathcal{C}_9^{\mathcal{R},S} \right)^* \right\} \operatorname{Re}[\mathcal{F}_{0,S}^{\text{res}} \mathcal{F}_{\parallel,P}^{\text{res},*}] \\
& + \frac{1}{4} \operatorname{Im} \rho_{3,P}^- (\operatorname{Im}[\mathcal{F}_{\parallel,P}^{\text{res}} \mathcal{F}_0^*] + \operatorname{Im}[\mathcal{F}_{0,P}^{\text{res}} \mathcal{F}_{\parallel}^*]) \\
& + \frac{1}{4} \operatorname{Im} \rho_{3,S}^- \operatorname{Im}[\mathcal{F}_{0,S}^{\text{res}} \mathcal{F}_{\parallel}^*] - \frac{1}{4} \operatorname{Re} \rho_{3,S}^- \operatorname{Re}[\mathcal{F}_{0,S}^{\text{res}} \mathcal{F}_{\parallel}^*] \\
& \left. + \frac{1}{4} \operatorname{Re} \rho_{3,P}^- (-\operatorname{Re}[\mathcal{F}_{\parallel,P}^{\text{res}} \mathcal{F}_0^*] - \operatorname{Re}[\mathcal{F}_{0,P}^{\text{res}} \mathcal{F}_{\parallel}^*]) \right] \sin \theta_{P_1}
\end{aligned} \tag{B.4}$$

$$\begin{aligned}
I_5 = & \left[+\operatorname{Re} \rho_2^+ \operatorname{Re}[\mathcal{F}_0 \mathcal{F}_{\perp}^*] + \operatorname{Im} \rho_2^- \operatorname{Im}[\mathcal{F}_0 \mathcal{F}_{\perp}^*] \right. \\
& + \frac{1}{2} \operatorname{Re} \rho_{4,P}^+ \operatorname{Re}[\mathcal{F}_{0,P}^{\text{res}} \mathcal{F}_{\perp}^*] - \frac{1}{2} \operatorname{Im} \rho_{4,P}^+ \operatorname{Im}[\mathcal{F}_{0,P}^{\text{res}} \mathcal{F}_{\perp}^*] \\
& + \frac{1}{2} \operatorname{Re} \rho_{4,S}^+ \operatorname{Re}[\mathcal{F}_{0,S}^{\text{res}} \mathcal{F}_{\perp}^*] - \frac{1}{2} \operatorname{Im} \rho_{4,S}^+ \operatorname{Im}[\mathcal{F}_{0,S}^{\text{res}} \mathcal{F}_{\perp}^*] \\
& \left. + \frac{1}{2} \operatorname{Re} \rho_{4,P}^- \operatorname{Re}[\mathcal{F}_{\perp,P}^{\text{res}} \mathcal{F}_0^*] - \frac{1}{2} \operatorname{Im} \rho_{4,P}^- \operatorname{Im}[\mathcal{F}_{\perp,P}^{\text{res}} \mathcal{F}_0^*] \right] \sin \theta_{P_1} ,
\end{aligned} \tag{B.5}$$

$$\begin{aligned}
I_6 = & \left[\operatorname{Im} \rho_2^- \operatorname{Im}[\mathcal{F}_{\perp} \mathcal{F}_{\parallel}^*] - \operatorname{Re} \rho_2^+ \operatorname{Re}[\mathcal{F}_{\parallel} \mathcal{F}_{\perp}^*] \right. \\
& + \frac{1}{2} \operatorname{Im} \rho_{4,P}^- \operatorname{Im}[\mathcal{F}_{\perp,P}^{\text{res}} \mathcal{F}_{\parallel}^*] - \frac{1}{2} \operatorname{Re} \rho_{4,P}^- \operatorname{Re}[\mathcal{F}_{\perp,P}^{\text{res}} \mathcal{F}_{\parallel}^*] \\
& \left. + \frac{1}{2} \operatorname{Im} \rho_{4,P}^+ \operatorname{Im}[\mathcal{F}_{\parallel,P}^{\text{res}} \mathcal{F}_{\perp}^*] - \frac{1}{2} \operatorname{Re} \rho_{4,P}^+ \operatorname{Re}[\mathcal{F}_{\parallel,P}^{\text{res}} \mathcal{F}_{\perp}^*] \right] \sin^2 \theta_{P_1} ,
\end{aligned} \tag{B.6}$$

$$\begin{aligned}
I_7 = & \left[+\delta \operatorname{Im}[\mathcal{F}_0 \mathcal{F}_{\parallel}^*] + \frac{1}{2} \operatorname{Re} \rho_{4,P}^- (-\operatorname{Im}[\mathcal{F}_{\parallel,P}^{\text{res}} \mathcal{F}_0^*] + \operatorname{Im}[\mathcal{F}_{0,P}^{\text{res}} \mathcal{F}_{\parallel}^*]) \right. \\
& + \frac{1}{2} \operatorname{Im} \rho_{4,P}^- (-\operatorname{Re}[\mathcal{F}_{\parallel,P}^{\text{res}} \mathcal{F}_0^*] + \operatorname{Re}[\mathcal{F}_{0,P}^{\text{res}} \mathcal{F}_{\parallel}^*]) \\
& \left. + \frac{1}{2} \operatorname{Re} \rho_{4,S}^- \operatorname{Im}[\mathcal{F}_{0,S}^{\text{res}} \mathcal{F}_{\parallel}^*] + \frac{1}{2} \operatorname{Im} \rho_{4,S}^- \operatorname{Re}[\mathcal{F}_{0,S}^{\text{res}} \mathcal{F}_{\parallel}^*] \right] \sin \theta_{P_1} ,
\end{aligned} \tag{B.7}$$

$$\begin{aligned}
I_8 = & \left[+\frac{1}{4} \left| \mathcal{C}_9^{\mathcal{R},P} \right|^2 \operatorname{Im}[\mathcal{F}_{\perp,P}^{\text{res}} \mathcal{F}_{0,P}^{\text{res},*}] + \frac{1}{2} \operatorname{Re} \rho_2^- \operatorname{Im}[\mathcal{F}_{\perp} \mathcal{F}_0^*] + \frac{1}{2} \operatorname{Im} \rho_2^+ \operatorname{Re}[\mathcal{F}_0 \mathcal{F}_{\perp}^*] \right. \\
& + \frac{1}{4} \operatorname{Re} \left\{ \mathcal{C}_9^{\mathcal{R},P} \left(\mathcal{C}_9^{\mathcal{R},S} \right)^* \right\} \operatorname{Im}[\mathcal{F}_{\perp,P}^{\text{res}} \mathcal{F}_{0,S}^{\text{res},*}] + \frac{1}{4} \operatorname{Im} \left\{ \mathcal{C}_9^{\mathcal{R},P} \left(\mathcal{C}_9^{\mathcal{R},S} \right)^* \right\} \operatorname{Re}[\mathcal{F}_{0,S}^{\text{res}} \mathcal{F}_{\perp,P}^{\text{res},*}] \\
& - \frac{1}{4} \operatorname{Im} \rho_{3,S}^+ \operatorname{Re}[\mathcal{F}_{0,S}^{\text{res}} \mathcal{F}_{\perp}^*] - \frac{1}{4} \operatorname{Re} \rho_{3,S}^+ \operatorname{Im}[\mathcal{F}_{0,S}^{\text{res}} \mathcal{F}_{\perp}^*] \\
& + \frac{1}{4} \operatorname{Im} \rho_{3,P}^- \operatorname{Re}[\mathcal{F}_{\perp,P}^{\text{res}} \mathcal{F}_0^*] + \frac{1}{4} \operatorname{Re} \rho_{3,P}^- \operatorname{Im}[\mathcal{F}_{\perp,P}^{\text{res}} \mathcal{F}_0^*] \\
& \left. - \frac{1}{4} \operatorname{Im} \rho_{3,P}^+ \operatorname{Re}[\mathcal{F}_{0,P}^{\text{res}} \mathcal{F}_{\perp}^*] - \frac{1}{4} \operatorname{Re} \rho_{3,P}^+ \operatorname{Im}[\mathcal{F}_{0,P}^{\text{res}} \mathcal{F}_{\perp}^*] \right] \sin \theta_{P_1} ,
\end{aligned} \tag{B.8}$$

$$\begin{aligned}
I_9 = & - \left[+\frac{1}{4} \left| \mathcal{C}_9^{\mathcal{R},P} \right|^2 \operatorname{Im}[\mathcal{F}_{\parallel,P}^{\text{res}} \mathcal{F}_{\perp,P}^{\text{res},*}] - \frac{1}{2} \operatorname{Im} \rho_2^+ \operatorname{Re}[\mathcal{F}_{\parallel} \mathcal{F}_{\perp}^*] + \frac{1}{2} \operatorname{Re} \rho_2^- \operatorname{Im}[\mathcal{F}_{\parallel} \mathcal{F}_{\perp}^*] \right. \\
& + \frac{1}{4} \operatorname{Re} \rho_{3,P}^+ \operatorname{Im}[\mathcal{F}_{\parallel,P}^{\text{res}} \mathcal{F}_{\perp}^*] + \frac{1}{4} \operatorname{Im} \rho_{3,P}^+ \operatorname{Re}[\mathcal{F}_{\parallel,P}^{\text{res}} \mathcal{F}_{\perp}^*] \\
& \left. - \frac{1}{4} \operatorname{Im} \rho_{3,P}^- \operatorname{Re}[\mathcal{F}_{\perp,P}^{\text{res}} \mathcal{F}_{\parallel}^*] - \frac{1}{4} \operatorname{Re} \rho_{3,P}^- \operatorname{Im}[\mathcal{F}_{\perp,P}^{\text{res}} \mathcal{F}_{\parallel}^*] \right] \sin^2 \theta_{P_1} ,
\end{aligned} \tag{B.9}$$

“good” bins	SM measurements	NP measurements	excluded measurements
$d\Gamma/dq^2 _{\sqrt{q^2}>0.6\text{ GeV}}$ [36]	$d\Gamma/dq^2$ [36]		
$d\Gamma/dp^2 _{\sqrt{p^2}<0.9\text{ GeV}}$ [36]	$d\Gamma/dp^2$ [36]		
\mathcal{B} with $\sqrt{q^2} \in \{[0.565-0.95], [0.95-1.1]\}$ GeV [40]	binned \mathcal{B} [40]		full- q^2 \mathcal{B} [40]
$\langle S_{2,3,4} \rangle$ [36]	binned $\langle S_{2,3,4} \rangle$ [36]		$\langle S_9 \rangle$ & full- q^2 $\langle S_{2,3,4} \rangle$ [36]
with $\sqrt{q^2} \in \{[0.565-0.78], [0.78-0.95], [0.95-1.02], [1.02-1.1]\}$ GeV		$\langle S_{5,6,7,8} \rangle$ & $\langle A_{2-0} \rangle$ [36]	full- q^2 $\langle S_{5,6,7,8} \rangle$ & $\langle A_{2-0} \rangle$ [36]
		with $\sqrt{q^2} \in \{[0.78-0.95], [0.95-1.02], [1.02-1.1]\}$ GeV	and $\sqrt{q^2} \in \{[< 0.565], [0.565-0.78]\}$ GeV

Table 6: Data on $D \rightarrow \pi^+\pi^-\mu^+\mu^-$ decays. We denote by SM measurements those dominated by SM contributions, whereas NP measurements are those that are negligible in the SM. The “good” bins are a subset of the SM measurements. Excluded measurements are those not used in any of our fits.

where the short-distance effects are encoded in

$$\begin{aligned}
\rho_1^\pm &= \frac{1}{2} [|\mathcal{C}_\pm^L|^2 + |\mathcal{C}_\pm^R|^2] = \left| \mathcal{C}_9^{\text{eff}} + \mathcal{C}_9 \pm \mathcal{C}'_9 \right|^2 + |\mathcal{C}_{10} \pm \mathcal{C}'_{10}|^2, \\
\delta\rho &= \frac{1}{4} [|\mathcal{C}_-^R|^2 - |\mathcal{C}_-^L|^2] = \text{Re} \left[\left(\mathcal{C}_9^{\text{eff}} + \mathcal{C}_9 - \mathcal{C}'_9 \right) (\mathcal{C}_{10} - \mathcal{C}'_{10})^* \right], \\
\text{Re}\rho_2^+ &= \frac{1}{4} \text{Re} [\mathcal{C}_+^R(\mathcal{C}_-^R)^* - \mathcal{C}_-^L(\mathcal{C}_+^L)^*] = \text{Re} \left[(\mathcal{C}_9^{\text{eff}} + \mathcal{C}_9) \mathcal{C}_{10}^* - \mathcal{C}'_9 \mathcal{C}'_{10} \right], \\
\text{Im}\rho_2^+ &= \frac{1}{4} \text{Im} [\mathcal{C}_+^R(\mathcal{C}_-^R)^* - \mathcal{C}_-^L(\mathcal{C}_+^L)^*] = \text{Im} \left[\mathcal{C}'_{10} \mathcal{C}_{10}^* + \mathcal{C}'_9 (\mathcal{C}_9 + \mathcal{C}_9^{\text{eff}})^* \right], \\
\text{Re}\rho_2^- &= \frac{1}{4} \text{Re} [\mathcal{C}_+^R(\mathcal{C}_-^R)^* + \mathcal{C}_-^L(\mathcal{C}_+^L)^*] = \frac{1}{2} \left[|\mathcal{C}_{10}|^2 - |\mathcal{C}'_{10}|^2 + \left| \mathcal{C}_9^{\text{eff}} + \mathcal{C}_9 \right|^2 - |\mathcal{C}'_9|^2 \right], \\
\text{Im}\rho_2^- &= \frac{1}{4} \text{Im} [\mathcal{C}_+^R(\mathcal{C}_-^R)^* + \mathcal{C}_-^L(\mathcal{C}_+^L)^*] = \text{Im} \left[\mathcal{C}'_{10} (\mathcal{C}_9^{\text{eff}} + \mathcal{C}_9)^* - \mathcal{C}_{10} \mathcal{C}'_9 \right], \\
\rho_{3,S/P}^\pm &= \frac{1}{2} \mathcal{C}_9^{\mathcal{R},S/P} ((\mathcal{C}_\pm^R)^* + (\mathcal{C}_\pm^L)^*) = \mathcal{C}_9^{\mathcal{R},S/P} (\mathcal{C}_9^* \pm \mathcal{C}'_9), \\
\rho_{4,S/P}^\pm &= \frac{1}{2} \mathcal{C}_9^{\mathcal{R},S/P} ((\mathcal{C}_\pm^R)^* - (\mathcal{C}_\pm^L)^*) = \mathcal{C}_9^{\mathcal{R},S/P} (\mathcal{C}_{10}^* \pm \mathcal{C}'_{10}).
\end{aligned} \tag{B.10}$$

In the SM besides the resonant contributions $\mathcal{C}_9^{\mathcal{R},S(P)}$ only one combination of couplings survives $\rho_1^\pm = 2\text{Re}\rho_2^- = |\mathcal{C}_9^{\text{eff}}|^2$, and $\delta\rho = \text{Re}\rho_2^+ = \text{Im}\rho_2^\pm = \rho_{3,S/P}^\pm = \rho_{4,S/P}^\pm = 0$. This is in stark contrast with corresponding $b \rightarrow d, s \ell^+\ell^-$ processes where two combinations are finite in the SM, $\rho_1^\pm = 2\text{Re}\rho_2^- = |\mathcal{C}_9^{\text{eff}}|^2 + |\mathcal{C}_{10}|^2$ and $\delta\rho = \text{Re}\rho_2^+ = \text{Re}\mathcal{C}_9^{\text{eff}}\mathcal{C}_{10}^*$ [37]. This difference originates from the GIM-condition in charm $\mathcal{C}_{10}^{\text{SM}} = 0$ and leads to the null tests with $I_{5,6,7}^{\text{SM}} = 0$.

C Input for SM and NP fits

Here we present in Tab. 6 the measurements used for the SM fits in Sec. 4.1 and NP fits in Sec. 4.2 taken from [36, 40]. We do not take angular observables S_i, A_i and branching ratio in the full q^2 region into account as these data are less sensitive and to avoid double-counting when using the q^2 -binned ones.

References

- [1] A. Cerri et al., *Report from Working Group 4: Opportunities in Flavour Physics at the HL-LHC and HE-LHC*, *CERN Yellow Rep. Monogr.* **7** (2019) 867 [[1812.07638](#)].
- [2] BELLE-II collaboration, *The Belle II Physics Book*, *PTEP* **2019** (2019) 123C01 [[1808.10567](#)]. [Erratum: PTEP 2020, 029201 (2020)].
- [3] BESIII collaboration, *Future Physics Programme of BESIII*, *Chin. Phys. C* **44** (2020) 040001 [[1912.05983](#)].
- [4] STCF WORKING GROUP collaboration, *Physics Program of the Super Tau-Charm Factory*, *PoS BEAUTY2020* (2021) 060.
- [5] FCC collaboration, *FCC Physics Opportunities: Future Circular Collider Conceptual Design Report Volume 1*, *Eur. Phys. J. C* **79** (2019) 474.
- [6] G. Burdman, E. Golowich, J.L. Hewett and S. Pakvasa, *Rare charm decays in the standard model and beyond*, *Phys. Rev. D* **66** (2002) 014009 [[hep-ph/0112235](#)].
- [7] S. Fajfer, P. Singer and J. Zupan, *The Radiative leptonic decays $D^0 \rightarrow e^+e^-\gamma, \mu^+\mu^-\gamma$ in the standard model and beyond*, *Eur. Phys. J. C* **27** (2003) 201 [[hep-ph/0209250](#)].
- [8] S. de Boer and G. Hiller, *Flavor and new physics opportunities with rare charm decays into leptons*, *Phys. Rev. D* **93** (2016) 074001 [[1510.00311](#)].
- [9] S. De Boer and G. Hiller, *Null tests from angular distributions in $D \rightarrow P_1 P_2 l^+ l^-$, $l = e, \mu$ decays on and off peak*, *Phys. Rev. D* **98** (2018) 035041 [[1805.08516](#)].
- [10] M. Golz, G. Hiller and T. Magorsch, *Pinning down $|\Delta_c| = |\Delta_u| = 1$ couplings with rare charm baryon decays*, *Eur. Phys. J. C* **82** (2022) 357 [[2202.02331](#)].
- [11] S. Meinel, $\Lambda_c \rightarrow N$ form factors from lattice QCD and phenomenology of $\Lambda_c \rightarrow n\ell^+\nu_\ell$ and $\Lambda_c \rightarrow p\mu^+\mu^-$ decays, *Phys. Rev. D* **97** (2018) 034511 [[1712.05783](#)].
- [12] FERMILAB LATTICE, MILC collaboration, *D-meson semileptonic decays to pseudoscalars from four-flavor lattice QCD*, *Phys. Rev. D* **107** (2023) 094516 [[2212.12648](#)].
- [13] LHCb collaboration, *Search for the rare decay of charmed baryon Λ_c^+ into the $p\mu^+\mu^-$ final state*, *Phys. Rev. D* **110** (2024) 052007 [[2407.11474](#)].
- [14] CMS collaboration, *Search for Rare Charm Decays Into Two Muons*, Tech. Rep. CMS-PAS-BPH-23-008, CERN, Geneva (2024).
- [15] C. Greub, T. Hurth, M. Misiak and D. Wyler, *The $c \rightarrow u\gamma$ contribution to weak radiative charm decay*, *Phys. Lett. B* **382** (1996) 415 [[hep-ph/9603417](#)].
- [16] S. de Boer, B. Müller and D. Seidel, *Higher-order Wilson coefficients for $c \rightarrow u$ transitions in the standard model*, *JHEP* **08** (2016) 091 [[1606.05521](#)].
- [17] K.G. Chetyrkin, M. Misiak and M. Munz, *Weak radiative B meson decay beyond leading logarithms*, *Phys. Lett. B* **400** (1997) 206 [[hep-ph/9612313](#)]. [Erratum: Phys.Lett.B 425, 414 (1998)].
- [18] C. Bobeth, M. Misiak and J. Urban, *Photonic penguins at two loops and m_t dependence of $BR[B \rightarrow X_s l^+ l^-]$* , *Nucl. Phys. B* **574** (2000) 291 [[hep-ph/9910220](#)].
- [19] P. Gambino, M. Gorbahn and U. Haisch, *Anomalous dimension matrix for radiative and rare semileptonic B decays up to three loops*, *Nucl. Phys. B* **673** (2003) 238 [[hep-ph/0306079](#)].

- [20] S. de Boer, *Probing the standard model with rare charm decays*, Ph.D. thesis, Tech. U., Dortmund (main), 2017. 10.17877/DE290R-18060.
- [21] T. Feldmann, B. Müller and D. Seidel, $D \rightarrow \rho \ell^+ \ell^-$ decays in the QCD factorization approach, *JHEP* **08** (2017) 105 [1705.05891].
- [22] A. Bharucha, D. Boito and C. Méaux, *Disentangling QCD and new physics in $D^+ \rightarrow \pi^+ \ell^+ \ell^-$* , *JHEP* **04** (2021) 158 [2011.12856].
- [23] N. Adolph, J. Brod and G. Hiller, *Radiative three-body D-meson decays in and beyond the standard model*, *Eur. Phys. J. C* **81** (2021) 45 [2009.14212].
- [24] LHCb collaboration, *Searches for 25 rare and forbidden decays of D^+ and D_s^+ mesons*, *JHEP* **06** (2021) 044 [2011.00217].
- [25] F. Kruger and L.M. Sehgal, *Lepton polarization in the decays $B \rightarrow X_s \mu^+ \mu^-$ and $B \rightarrow X_s \tau^+ \tau^-$* , *Phys. Lett. B* **380** (1996) 199 [hep-ph/9603237].
- [26] M. Golz, G. Hiller and T. Magorsch, *Probing for new physics with rare charm baryon ($\Lambda_c, \Xi_c, \Omega_c$) decays*, *JHEP* **09** (2021) 208 [2107.13010].
- [27] C. Bobeth, G. Hiller and G. Piranishvili, *Angular distributions of $\bar{B} \rightarrow \bar{K} \ell^+ \ell^-$ decays*, *JHEP* **12** (2007) 040 [0709.4174].
- [28] R. Bause, M. Golz, G. Hiller and A. Tayduganov, *The new physics reach of null tests with $D \rightarrow \pi \ell \ell$ and $D_s \rightarrow K \ell \ell$ decays*, *Eur. Phys. J. C* **80** (2020) 65 [1909.11108]. [Erratum: Eur.Phys.J.C 81, 219 (2021)].
- [29] ETM collaboration, *Tensor form factor of $D \rightarrow \pi(K) \ell \nu$ and $D \rightarrow \pi(K) \ell \ell$ decays with $N_f = 2 + 1 + 1$ twisted-mass fermions*, *Phys. Rev. D* **98** (2018) 014516 [1803.04807].
- [30] H. Gisbert, M. Golz and D.S. Mitzel, *Theoretical and experimental status of rare charm decays*, *Mod. Phys. Lett. A* **36** (2021) 2130002 [2011.09478].
- [31] BELLE collaboration, *Search for the rare decay $D^0 \rightarrow \gamma \gamma$ at Belle*, *Phys. Rev. D* **93** (2016) 051102 [1512.02992].
- [32] FLAVOUR LATTICE AVERAGING GROUP (FLAG) collaboration, *FLAG Review 2021*, *Eur. Phys. J. C* **82** (2022) 869 [2111.09849].
- [33] S. Fajfer, P. Singer and J. Zupan, *The Rare decay $D^0 \rightarrow \gamma \gamma$* , *Phys. Rev. D* **64** (2001) 074008 [hep-ph/0104236].
- [34] PARTICLE DATA GROUP collaboration, *Review of Particle Physics*, *PTEP* **2022** (2022) 083C01.
- [35] S. Fajfer and N. Košnik, *Prospects of discovering new physics in rare charm decays*, *Eur. Phys. J. C* **75** (2015) 567 [1510.00965].
- [36] LHCb collaboration, *Angular Analysis of $D^0 \rightarrow \pi^+ \pi^- \mu^+ \mu^-$ and $D^0 \rightarrow K^+ K^- \mu^+ \mu^-$ Decays and Search for CP Violation*, *Phys. Rev. Lett.* **128** (2022) 221801 [2111.03327].
- [37] D. Das, G. Hiller, M. Jung and A. Shires, *The $\bar{B} \rightarrow \bar{K} \pi \ell \ell$ and $\bar{B}_s \rightarrow \bar{K} K \ell \ell$ distributions at low hadronic recoil*, *JHEP* **09** (2014) 109 [1406.6681].
- [38] C.L.Y. Lee, M. Lu and M.B. Wise, *$B(l_4)$ and $D(l_4)$ decay*, *Phys. Rev. D* **46** (1992) 5040.
- [39] S. Fajfer, E. Solomonidi and L. Vale Silva, *S-wave contribution to rare $D^0 \rightarrow \pi^+ \pi^- \ell^+ \ell^-$ decays in the standard model and sensitivity to new physics*, *Phys. Rev. D* **109** (2024) 3 [2312.07501].

- [40] LHCb collaboration, *Observation of D^0 meson decays to $\pi^+\pi^-\mu^+\mu^-$ and $K^+K^-\mu^+\mu^-$ final states*, *Phys. Rev. Lett.* **119** (2017) 181805 [[1707.08377](#)].
- [41] R. Bause, H. Gisbert, M. Golz and G. Hiller, *Model-independent analysis of $b \rightarrow d$ processes*, *Eur. Phys. J. C* **83** (2023) 419 [[2209.04457](#)].
- [42] L. Cappiello, O. Cata and G. D'Ambrosio, *Standard Model prediction and new physics tests for $D^0 \rightarrow h^+h^-\ell^+\ell^-$ ($h = \pi, K : \ell = e, \mu$)*, *JHEP* **04** (2013) 135 [[1209.4235](#)].
- [43] R. Bause, H. Gisbert, M. Golz and G. Hiller, *Interplay of dineutrino modes with semileptonic rare B -decays*, *JHEP* **12** (2021) 061 [[2109.01675](#)].
- [44] J. Fuentes-Martin, A. Greljo, J. Martin Camalich and J.D. Ruiz-Alvarez, *Charm physics confronts high- p_T lepton tails*, *JHEP* **11** (2020) 080 [[2003.12421](#)].
- [45] R. Bause, H. Gisbert, M. Golz and G. Hiller, *Lepton universality and lepton flavor conservation tests with dineutrino modes*, *Eur. Phys. J. C* **82** (2022) 164 [[2007.05001](#)].
- [46] D. Melikhov and B. Stech, *Weak form-factors for heavy meson decays: An Update*, *Phys. Rev. D* **62** (2000) 014006 [[hep-ph/0001113](#)].
- [47] BESIII collaboration, *Observation of $D^+ \rightarrow f_0(500)e^+\nu_e$ and Improved Measurements of $D \rightarrow \rho e^+\nu_e$* , *Phys. Rev. Lett.* **122** (2019) 062001 [[1809.06496](#)].
- [48] BESIII collaboration, *A New Look at the Scalar Meson $f_0(500)$ via $D^+ \rightarrow \pi^+\pi^-\ell^+\nu_\ell$ Decays*, [2401.13225](#).